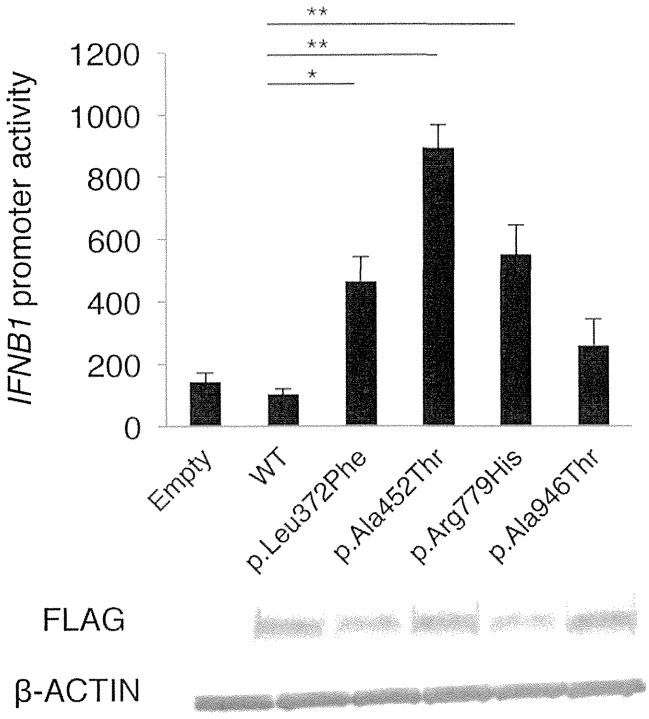

Figure 3. The Effects of the Three MDA5 Variants on *IFNB1* Expression

Huh7 cells were transfected with a reporter gene containing *IFNB1* promoter (p-55C1B Luc), an empty vector (BOS), and expression vectors for FLAG-tagged human wild-type *IFIH1*, c.2836G>A polymorphism (p.Ala946Thr) in the GWASs, and the identified *IFIH1* mutants. Luciferase activity was measured 48 hr after transfection, and the MDA5 protein accumulation was examined by immunoblotting as previously described.[15] FLAG indicates the accumulation of FLAG-tagged MDA5. Each experiment was performed in triplicate and data are mean ± SEM. Shown is a representative of two with consistent results. Statistical significance was determined by Student's t test. *$p < 0.05$, **$p < 0.01$.

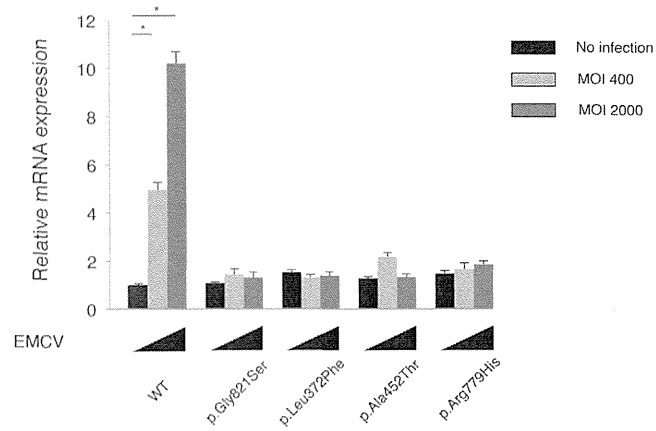

Figure 4. *Ifnb* mRNA Levels in *Ifih1*-Deficient MEFs Expressing *IFIH1* Mutants

The MEFs were infected with retroviruses encoding mouse wild-type *Ifih1*, mouse *Ifih1* with c.2461G>A (p.Gly821Ser) (RefSeq NM_027835.3) mutation, or the three AGS mutants of human *IFIH1*. At 48 hr after the retroviral infection, these MEFs were infected with indicated multiplicity of infection (MOI) of EMCV for 6 hr, and *Ifnb* mRNA levels were measured by qRT-PCR. The relative abundance of each transcript was normalized to the expression level of 18S ribosomal RNA. Data are shown as mean ± SEM of triplicate samples. Shown is a representative of two independent experiments. Statistical significance was determined by Student's t test, *$p < 0.001$. The expression of the retrovirally transduced FLAG-tagged constructs was confirmed by immunoblotting (Figure S5).

In conclusion, we identified mutations in *IFIH1* as a cause of AGS. The individuals with the *IFIH1* mutations showed encephalopathy typical of AGS as well as the type I interferon signature with autoimmune phenotypes, but lacked the chilblains. Further analysis remains to elucidate the mechanism of how the *IFIH1* mutations identified in AGS cause the type I interferon overproduction.

Supplemental Data

Supplemental Data include five figures and two tables and can be found with this article online at http://dx.doi.org/10.1016/j.ajhg.2014.06.007.

Acknowledgments

We are very grateful to Y. Takaoka (Kyoto University) and E. Abe (RIKEN Center for Integrative Medical Sciences) for their technical assistance on Sanger sequencing, to E. Hirano (Kyoto University) for her technical assistance on functional analyses of the AGS mutants, to M. Takazawa (Kazusa DNA Research Institute) for his contribution to exome data analysis, and to T. Taylor for his critical reading of the manuscript. This work was supported by the Platform for Drug Discovery, Informatics, and Structural Life Science from the Ministry of Education, Culture, Sports, Science and Technology, Japan. This work was supported by Grants-in-aid for Scientific Research from the Japanese Ministry of Health, Labor and Welfare and the Japanese Ministry of Education, Culture, Sports, Science, Technology (MEXT).

Received: March 1, 2014
Accepted: June 11, 2014
Published: July 3, 2014

Web Resources

The URLs for the data presented herein are as follows:

Burrows-Wheeler Aligner, http://bio-bwa.sourceforge.net/
ClustalW2, http://www.ebi.ac.uk/Tools/msa/clustalw2/
dbSNP, http://www.ncbi.nlm.nih.gov/projects/SNP/
EMDataBank, http://www.emdatabank.org/index.html
GATK, http://www.broadinstitute.org/gatk/
Human Genetic Variation Database (HGVD), http://www.genome.med.kyoto-u.ac.jp/SnpDB/
MutationTaster, http://www.mutationtaster.org/
Online Mendelian Inheritance in Man (OMIM), http://www.omim.org/
PolyPhen-2, http://www.genetics.bwh.harvard.edu/pph2/
PROVEAN, http://provean.jcvi.org/index.php
RCSB Protein Data Bank, http://www.rcsb.org/pdb/home/home.do
RefSeq, http://www.ncbi.nlm.nih.gov/RefSeq
SIFT, http://sift.bii.a-star.edu.sg/

References

1. Chahwan, C., and Chahwan, R. (2012). Aicardi-Goutieres syndrome: from patients to genes and beyond. Clin. Genet. *81*, 413–420.
2. Ramantani, G., Kohlhase, J., Hertzberg, C., Innes, A.M., Engel, K., Hunger, S., Borozdin, W., Mah, J.K., Ungerath, K., Walkenhorst, H., et al. (2010). Expanding the phenotypic spectrum of lupus erythematosus in Aicardi-Goutières syndrome. Arthritis Rheum. *62*, 1469–1477.
3. Orcesi, S., La Piana, R., and Fazzi, E. (2009). Aicardi-Goutieres syndrome. Br. Med. Bull. *89*, 183–201.
4. Rice, G., Patrick, T., Parmar, R., Taylor, C.F., Aeby, A., Aicardi, J., Artuch, R., Montalto, S.A., Bacino, C.A., Barroso, B., et al. (2007). Clinical and molecular phenotype of Aicardi-Goutieres syndrome. Am. J. Hum. Genet. *81*, 713–725.
5. Blau, N., Bonafé, L., Krägeloh-Mann, I., Thöny, B., Kierat, L., Häusler, M., and Ramaekers, V. (2003). Cerebrospinal fluid pterins and folates in Aicardi-Goutières syndrome: a new phenotype. Neurology *61*, 642–647.
6. Crow, Y.J., Hayward, B.E., Parmar, R., Robins, P., Leitch, A., Ali, M., Black, D.N., van Bokhoven, H., Brunner, H.G., Hamel, B.C., et al. (2006). Mutations in the gene encoding the 3′-5′ DNA exonuclease TREX1 cause Aicardi-Goutières syndrome at the AGS1 locus. Nat. Genet. *38*, 917–920.
7. Crow, Y.J., Leitch, A., Hayward, B.E., Garner, A., Parmar, R., Griffith, E., Ali, M., Semple, C., Aicardi, J., Babul-Hirji, R., et al. (2006). Mutations in genes encoding ribonuclease H2 subunits cause Aicardi-Goutières syndrome and mimic congenital viral brain infection. Nat. Genet. *38*, 910–916.
8. Rice, G.I., Bond, J., Asipu, A., Brunette, R.L., Manfield, I.W., Carr, I.M., Fuller, J.C., Jackson, R.M., Lamb, T., Briggs, T.A., et al. (2009). Mutations involved in Aicardi-Goutières syndrome implicate SAMHD1 as regulator of the innate immune response. Nat. Genet. *41*, 829–832.
9. Rice, G.I., Kasher, P.R., Forte, G.M., Mannion, N.M., Greenwood, S.M., Szynkiewicz, M., Dickerson, J.E., Bhaskar, S.S., Zampini, M., Briggs, T.A., et al. (2012). Mutations in ADAR1 cause Aicardi-Goutières syndrome associated with a type I interferon signature. Nat. Genet. *44*, 1243–1248.
10. Abe, J., Nakamura, K., Nishikomori, R., Kato, M., Mitsuiki, N., Izawa, K., Awaya, T., Kawai, T., Yasumi, T., Toyoshima, I., et al. (2014). A nationwide survey of Aicardi-Goutieres syndrome patients identifies a strong association between dominant TREX1 mutations and chilblain lesions: Japanese cohort study. Rheumatology *53*, 448–458.
11. Yoneyama, M., and Fujita, T. (2009). RNA recognition and signal transduction by RIG-I-like receptors. Immunol. Rev. *227*, 54–65.
12. Wu, B., Peisley, A., Richards, C., Yao, H., Zeng, X., Lin, C., Chu, F., Walz, T., and Hur, S. (2013). Structural basis for dsRNA recognition, filament formation, and antiviral signal activation by MDA5. Cell *152*, 276–289.
13. Berke, I.C., Yu, X., Modis, Y., and Egelman, E.H. (2012). MDA5 assembles into a polar helical filament on dsRNA. Proc. Natl. Acad. Sci. USA *109*, 18437–18441.
14. Rice, G.I., Forte, G.M., Szynkiewicz, M., Chase, D.S., Aeby, A., Abdel-Hamid, M.S., Ackroyd, S., Allcock, R., Bailey, K.M., Balottin, U., et al. (2013). Assessment of interferon-related biomarkers in Aicardi-Goutières syndrome associated with mutations in TREX1, RNASEH2A, RNASEH2B, RNASEH2C, SAMHD1, and ADAR: a case-control study. Lancet Neurol. *12*, 1159–1169.
15. Funabiki, M., Kato, H., Miyachi, Y., Toki, H., Motegi, H., Inoue, M., Minowa, O., Yoshida, A., Deguchi, K., Sato, H., et al. (2014). Autoimmune disorders associated with gain of function of the intracellular sensor MDA5. Immunity *40*, 199–212.
16. Smyth, D.J., Cooper, J.D., Bailey, R., Field, S., Burren, O., Smink, L.J., Guja, C., Ionescu-Tirgoviste, C., Widmer, B., Dunger, D.B., et al. (2006). A genome-wide association study of nonsynonymous SNPs identifies a type 1 diabetes locus in the interferon-induced helicase (IFIH1) region. Nat. Genet. *38*, 617–619.
17. Gateva, V., Sandling, J.K., Hom, G., Taylor, K.E., Chung, S.A., Sun, X., Ortmann, W., Kosoy, R., Ferreira, R.C., Nordmark, G., et al. (2009). A large-scale replication study identifies TNIP1, PRDM1, JAZF1, UHRF1BP1 and IL10 as risk loci for systemic lupus erythematosus. Nat. Genet. *41*, 1228–1233.
18. Strange, A., Capon, F., Spencer, C.C., Knight, J., Weale, M.E., Allen, M.H., Barton, A., Band, G., Bellenguez, C., Bergboer, J.G., et al.; Genetic Analysis of Psoriasis Consortium & the Wellcome Trust Case Control Consortium 2 (2010). A genome-wide association study identifies new psoriasis susceptibility loci and an interaction between HLA-C and ERAP1. Nat. Genet. *42*, 985–990.
19. Jin, Y., Birlea, S.A., Fain, P.R., Ferrara, T.M., Ben, S., Riccardi, S.L., Cole, J.B., Gowan, K., Holland, P.J., Bennett, D.C., et al. (2012). Genome-wide association analyses identify 13 new susceptibility loci for generalized vitiligo. Nat. Genet. *44*, 676–680.
20. Bennett, L., Palucka, A.K., Arce, E., Cantrell, V., Borvak, J., Banchereau, J., and Pascual, V. (2003). Interferon and granulopoiesis signatures in systemic lupus erythematosus blood. J. Exp. Med. *197*, 711–723.
21. Lee-Kirsch, M.A., Gong, M., Chowdhury, D., Senenko, L., Engel, K., Lee, Y.A., de Silva, U., Bailey, S.L., Witte, T., Vyse, T.J., et al. (2007). Mutations in the gene encoding the 3′-5′ DNA exonuclease TREX1 are associated with systemic lupus erythematosus. Nat. Genet. *39*, 1065–1067.
22. Kato, H., Takeuchi, O., Sato, S., Yoneyama, M., Yamamoto, M., Matsui, K., Uematsu, S., Jung, A., Kawai, T., Ishii, K.J., et al. (2006). Differential roles of MDA5 and RIG-I helicases in the recognition of RNA viruses. Nature *441*, 101–105.
23. Rice, G.I., del Toro Duany, Y., Jenkinson, E.M., Forte, G.M., Anderson, B.H., Ariaudo, G., Bader-Meunier, B., Baildam, E.M., Battini, R., Beresford, M.W., et al. (2014). Gain-of-function mutations in IFIH1 cause a spectrum of human disease phenotypes associated with upregulated type I interferon signaling. Nat. Genet. *46*, 503–509.

OPEN ACCESS
CellPress

Cell Reports

Single-Cell Imaging of Caspase-1 Dynamics Reveals an All-or-None Inflammasome Signaling Response

Ting Liu,[1] Yoshifumi Yamaguchi,[1,2,*] Yoshitaka Shirasaki,[3] Koichi Shikada,[1] Mai Yamagishi,[3] Katsuaki Hoshino,[4,5,6] Tsuneyasu Kaisho,[5,6,12] Kiwamu Takemoto,[2,7] Toshihiko Suzuki,[8] Erina Kuranaga,[9] Osamu Ohara,[3,10] and Masayuki Miura[1,11,*]

[1]Department of Genetics, Graduate School of Pharmaceutical Sciences, The University of Tokyo, Bunkyo-ku, Tokyo 113-0033, Japan
[2]PRESTO, Japan Science and Technology Agency, Chiyoda-ku, Tokyo 102-0076, Japan
[3]Laboratory for Integrative Genomics, RIKEN Center for Integrative Medical Sciences (IMS-RCAI), Yokohama, Kanagawa 230-0045, Japan
[4]Department of Immunology, Faculty of Medicine, Kagawa University, Kita-gun, Kagawa 761-0793, Japan
[5]Laboratory for Immune Regulation, World Premier International Research Center Initiative Immunology Frontier Research Center, Osaka University, Suita, Osaka 565-0861, Japan
[6]Laboratory for Host Defense, RIKEN Research Center for Allergy and Immunology, Yokohama, Kanagawa 230-0045, Japan
[7]Department of Physiology, Graduate School of Medicine, Yokohama City University, Yokohama, Kanagawa 236-0004, Japan
[8]Department of Molecular Bacteriology and Immunology, Graduate School of Medicine, University of the Ryukyus, Nakagami-gun, Okinawa 903-0125, Japan
[9]Laboratory for Histogenetic Dynamics, RIKEN Center for Developmental Biology, Chuo-ku, Kobe 650-0047, Japan
[10]Department of Human Genome Research, Kazusa DNA Research Institute, Kisarazu, Chiba 292-0818, Japan
[11]CREST, Japan Science and Technology Agency, Chiyoda-ku, Tokyo 102-0076, Japan
[12]Present address: Department of Immunology, Institute of Advanced Medicine, Wakayama Medical University, 811-1 Kimiidera, Wakayama, Wakayama 641-8509, Japan
*Correspondence: bunbun@mol.f.u-tokyo.ac.jp (Y.Y.), miura@mol.f.u-tokyo.ac.jp (M.M.)
http://dx.doi.org/10.1016/j.celrep.2014.07.012

SUMMARY

Inflammasome-mediated caspase-1 activation is involved in cell death and the secretion of the proinflammatory cytokine interleukin-1β (IL-1β). Although the dynamics of caspase-1 activation, IL-1β secretion, and cell death have been examined with bulk assays in population-level studies, they remain poorly understood at the single-cell level. In this study, we conducted single-cell imaging using a genetic fluorescence resonance energy transfer sensor that detects caspase-1 activation. We determined that caspase-1 exhibits all-or-none (digital) activation at the single-cell level, with similar activation kinetics irrespective of the type of inflammasome or the intensity of the stimulus. Real-time concurrent detection of caspase-1 activation and IL-1β release demonstrated that dead macrophages containing activated caspase-1 release a local burst of IL-1β in a digital manner, which identified these macrophages as the main source of IL-1β within cell populations. Our results highlight the value of single-cell analysis in enhancing understanding of the inflammasome system and chronic inflammatory diseases.

INTRODUCTION

Macrophages (MΦs) play crucial roles in homeostasis by clearing dead cells and connecting innate immunity with adaptive immunity (Mosser and Edwards, 2008). When MΦs detect pathogen-associated molecular patterns (PAMPs) derived from infection or damage-associated molecular patterns (DAMPs) originating from injured tissues, they secrete various types of cytokines to induce inflammation or tissue repair. Interleukin-1β (IL-1β) is a key cytokine that evokes an inflammatory response, and its secretion is mainly regulated by caspase-1, a member of the cysteine-protease family of caspases (Denes et al., 2012).

Caspase-1 is synthesized as an inactive zymogen and then activated via proteolytic cleavage, a process regulated by intracellular multiprotein complexes called inflammasomes (Martinon et al., 2002; Rathinam et al., 2012); the inflammasomes detect PAMPs and DAMPs by using distinct intracellular pattern-recognition receptors such as NLRP3 (Nod-like receptor family, pyrin domain containing 3), NLRC4 (Nod-like receptor family, CARD domain containing 4), and AIM2 (absent in melanoma 2) (Martinon et al., 2002; Rathinam et al., 2012). When PAMPs or DAMPs are detected, procaspase-1 is recruited directly through interactions between the pattern-recognition receptors and procaspase-1 or indirectly through adaptor proteins such as ASC (apoptosis-associated speck-like protein containing CARD) (Schroder and Tschopp, 2010). The recruited procaspase-1 is activated through autoproteolytic cleavage mediated by proximity-induced multimerization. In addition to regulating proinflammatory cytokines, caspase-1 activation has been shown to cause cell death (Miura et al., 1993). In certain cases, caspase-1 is necessary for the execution of necrotic inflammatory cell death, called pyroptosis, in MΦs in response to intracellular bacterial infection (Fink and Cookson, 2005; Miao et al., 2010). However, in other cases, although caspase-1 is activated in response to various PAMPs or DAMPs, deleting or inhibiting caspase-1 is

insufficient for preventing cell death (Broz et al., 2010; Pierini et al., 2012).

Given the aforementioned studies, the activation of most inflammasomes is considered to typically converge on caspase-1 activation, which couples the secretion of the proinflammatory cytokine IL-1β and cell death. However, most of the information on inflammasomes and caspase-1 has been obtained from population-level studies conducted using bulk assays such as western blotting and ELISA, mainly because of technical limitations and because of the unique characteristics of caspase-1 such as rapid secretion after activation and rapid inactivation (Keller et al., 2008; Walsh et al., 2011). Emerging evidence suggests that population data do not faithfully reflect how single cells respond to stimuli (Tay et al., 2010). Thus, the mechanism through which individual cells activate caspase-1 by means of distinct inflammasomes and secrete IL-1β in response to inflammatory stimuli remains unclear. Determining signaling dynamics at the single-cell level not only expands the general understanding of how biological systems work but also complements in vivo studies that examine cells residing in complex contexts (Tay et al., 2010). Single-cell measurement of caspase-1 activity at high spatiotemporal resolution is required to fully understand the dynamics of caspase-1 activation and the direct relationship between caspase-1 activation and its associated outcomes, IL-1β secretion and cell death.

To monitor caspase-1 activity at the single-cell level, we developed SCAT1, a genetically encoded fluorescent sensor for detecting caspase-1 activation based on fluorescence resonance energy transfer (FRET). Using peritoneal MΦs (PMΦs) obtained from transgenic mice expressing SCAT1, we determined that caspase-1 is activated in a digital manner at the single-cell level in response to various types of inflammasomes. Interestingly, the kinetics of caspase-1 activation was similar regardless of the strength and type of stimuli. Moreover, by combining the SCAT1 system and a newly developed technique to measure protein secretion at single-cell resolution, we identified dying MΦs that contained activated caspase-1 as the source of secreted IL-1β in PMΦ populations.

RESULTS

Real-Time Detection of Caspase-1 Activation through the NLRP3 Inflammasome with SCAT1, a Genetically Encoded Probe Developed for Monitoring Caspase-1 Activation

Probes based on FRET technology can provide critical information on the dynamics and activities of endogenous enzymes in living cells (Aoki et al., 2013). We previously generated a genetically encoded probe called SCAT3 (sensor for caspase-3 activation based on FRET) and monitored apoptotic caspase-3 activation in vitro and in vivo (Kuranaga et al., 2011; Nakajima et al., 2011; Takemoto et al., 2003, 2007; Yamaguchi et al., 2011). SCAT comprises 2 fluorescent proteins—enhanced cyan fluorescent protein (ECFP) and Venus—that are connected by a linker sequence that contains caspase cleavage sites (Figure 1A). Upon caspase activation, the linker is cleaved and the FRET between ECFP and Venus is disrupted, which can be detected in real time with fluorescence microscopy. To detect real-time activation of caspase-1, we constructed SCAT1 containing YVAD (a consensus peptide sequence preferentially cleaved by caspase-1) in its linker sequence instead of the DEVD sequence present in SCAT3 (Figure 1A).

The results of in vitro cleavage assays demonstrated that SCAT1 was preferentially cleaved by activated human caspase-1 (Figure S1A). Notably, SCAT1 was barely processed by activated human caspase-4 and caspase-5, which represent potential functional orthologs of murine caspase-11. The specificity of SCAT1 cleavage upon caspase-1 activation was also confirmed in living cells with the caspase-1-specific inhibitor z-YVAD-fmk or by genetic deletion of caspase-1/11 (Figure S1B; see below for a detailed explanation). We generated a gene-targeting mouse line in which the CAG-promoter-loxP-STOP-loxP-SCAT1 gene cassette was knocked into the Rosa26 locus. In this knockin mouse line, SCAT1 expression depended on Cre recombinase expression (Figure S1C); by mating these mice with mice that ubiquitously expressed Cre, we generated mice that expressed SCAT1 in all tissues. We obtained peritoneal MΦs (PMΦs) expressing SCAT1 from these mice. The possibility that overexpressed SCAT1, an exogenous substrate of caspase-1, might prevent the endogenous function of caspase-1 was excluded by our observation that IL-1β secretion and caspase-1 cleavage occurred similarly in PMΦs derived from SCAT1$^-$ (wild-type) and SCAT1$^+$ mice after inflammasome-activation stimulated with lipopolysaccharide (LPS) + ATP or poly(dA:dT) (Figures S1D and S1E).

Various pathogenic, endogenous, and environmental stimuli can activate the NLRP3 inflammasome after priming with LPS or other Toll-like receptor ligands (Latz et al., 2013). We examined whether SCAT1 can enable real-time detection of caspase-1 activation induced by canonical activators of the NLRP3 inflammasome at the single-cell level. PMΦs collected from SCAT1 knockin mice were stimulated with an environmental danger signal (silica crystals) after LPS priming and were observed continuously under a confocal microscope to monitor the time course of changes in SCAT1 (Venus and ECFP) intensities. The SCAT1 Venus/ECFP (V/C) ratio decreased rapidly and dramatically (Figures 1B and 1C; Movie S1) in some of the cells after stimulation, indicating that caspase-1 was activated; the time of caspase-1 activation varied among cells (Figures S2A and S2B). Moreover, adding the caspase-1-specific inhibitor z-YVAD-fmk abolished the dramatic reduction in the SCAT1 V/C ratio and the cleavage of SCAT1 (Figures 1B, 1C, S1B, S2A, and S2B; Movie S1), indicating that SCAT1 accurately detected caspase-1 activation. We also confirmed that apoptotic caspases were not activated in PMΦs stimulated with LPS + silica; SCAT3, the indicator of caspase-3 activation, did not detect apoptotic activation of caspases in these PMΦs (Figure S2C).

Time-lapse imaging showed that SCAT1 fluorescence disappeared after caspase-1 activation, but the fluorescence was lost even when caspase-1 activation was prevented by its inhibitor (Figure 1B). This loss of fluorescence indicated cell death accompanying membrane rupture because it coincided with the cells becoming positive for TO-PRO-3 or propidium iodide staining (Figure 1D; Movie S1). These data indicated that SCAT1 can faithfully detect NLRP3 inflammasome-induced activation of caspase-1 and subsequent cell death in real time at the single-cell level. Interestingly, the dynamics of SCAT1 V/C ratios

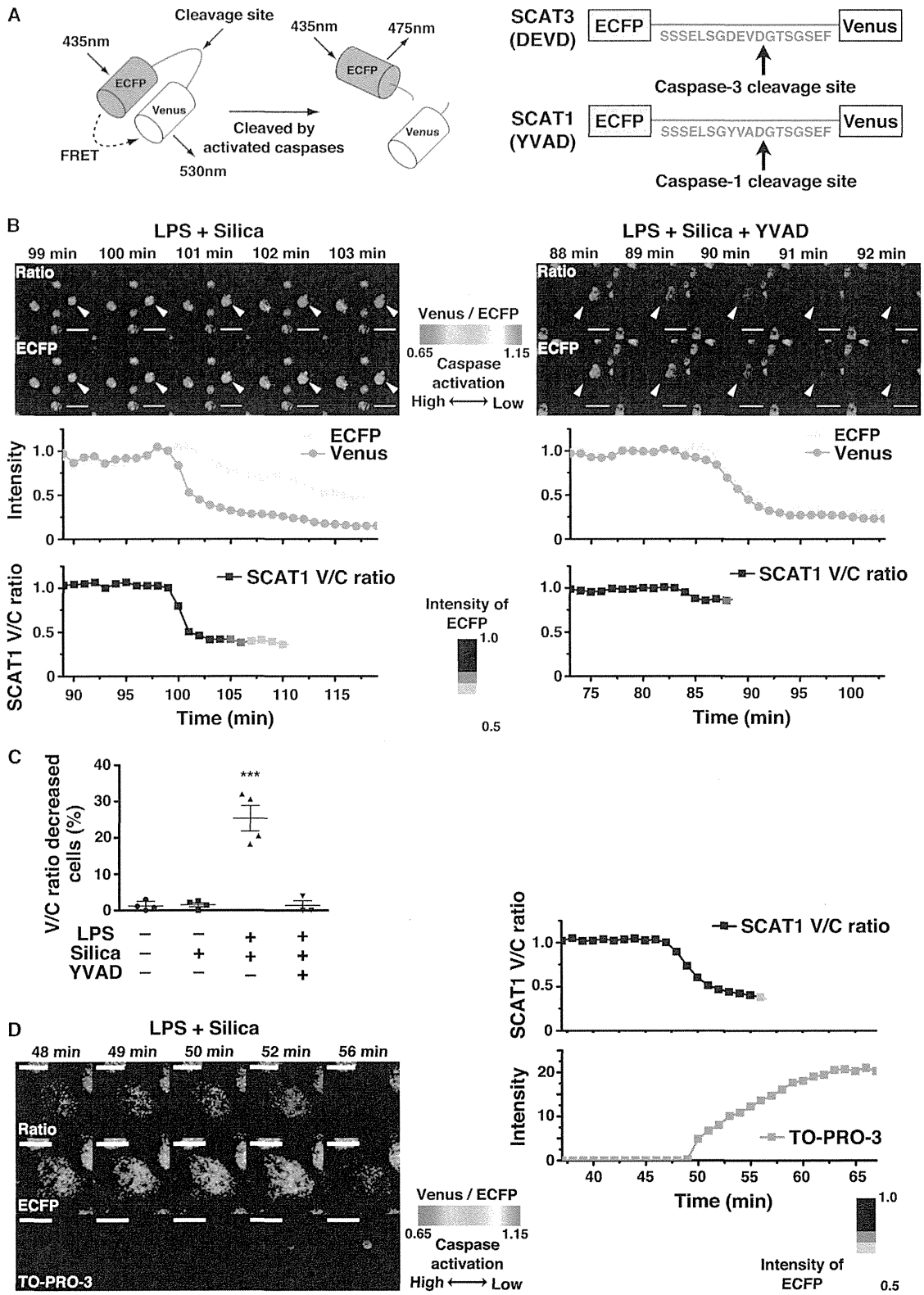

(legend on next page)

in PMΦs exhibited only two patterns: no decrease or dramatic decrease.

Real-Time Detection of Caspase-1 Activation via AIM2 and NLRC4 Inflammasomes

Next, we determined whether SCAT1 detects caspase-1 activation via two other types of inflammasomes, AIM2 and NLRC4, in addition to activation by the NLRP3 inflammasome. The AIM2 inflammasome is activated by poly(dA:dT) transfection with or without LPS priming (Fernandes-Alnemri et al., 2009; Hornung et al., 2009). The SCAT1 V/C ratio dramatically decreased in some PMΦs after poly(dA:dT) transfection in a manner independent of LPS priming (Figures 2A, 2B, and S3A–S3C; Movie S2). This decrease was abolished when the caspase-1 inhibitor was added to SCAT1$^+$ PMΦs or SCAT1$^+$ caspase-1/11-deficient PMΦs (Figures 2A, 2B, and S3B–S3D; Movie S2) (Kayagaki et al., 2011; Kuida et al., 1995). Regardless of the presence or absence of caspase-1 activity, cell death occurred, which was indicated by the disappearance of SCAT1 fluorescence (shown as a loss of ECFP intensity in the SCAT1 V/C ratio graphs in Figures 1B, 1D, 2A, 2C, S2C, S3A, S4A, and S4B).

The NLRC4 inflammasome is activated by pathogenic proteins derived from various bacteria, including *Salmonella* serotype Typhimurium, *Legionella pneumophila*, and *Pseudomonas aeruginosa* (Franchi et al., 2012). SCAT1 V/C ratios rapidly decreased after infection with *S.* Typhimurium SL1344 (Figure 2C), but not after infection with *S.* TyphimuriumΔ invGsseD (a strain that exhibits little capability to induce inflammasomes) or when caspase-1 was inhibited (Figures S4A and S4B; Movie S3). Taken together, these data indicate that SCAT1 detects caspase-1 activation and subsequent cell death that occur via activation of the AIM2, NLRC4, and NLRP3 inflammasomes.

Nearly Identical Kinetics of Caspase-1 Activation and the Resulting Inflammatory Cell Death in Response to Distinct Stimuli

The results of our SCAT1 imaging suggested that caspase-1 activation is a digital, all-or-none response. To quantify and characterize the caspase-1 activation further, we conducted kinetic analyses of caspase-1 activation at the single-cell level. We first investigated whether the kinetics of caspase-1 activation varied in relation to the distinct types of inflammasomes at the single-cell level. The AIM2, NLRP3, and NRLC4 inflammasomes stimulated similar time courses of change in the SCAT1 V/C ratio in response to poly(dA:dT), silica, and *S.* Typhimurium (Figure 3A).

Next, we examined whether varying the stimulus intensity affects the dynamics of caspase-1 activation at the single-cell level. We used poly(dA:dT) as a model stimulus because it does not require LPS priming, which may induce unexpected disparities in cellular competence to stimulus. We transfected poly(dA:dT) into PMΦs at five concentrations and measured the kinetics of caspase-1 activation. The results revealed that the kinetics of caspase-1 activation (change in the relative SCAT1 V/C ratio over time) was similar across all stimulus intensities (Figure 3B). However, stimulus intensity affected the number of PMΦs that contained activated caspase-1 and subsequently underwent cell death, and this number increased in a dose-dependent manner (Figure 3C). Moreover, IL-1β production measured using ELISA, a bulk assay, exhibited a similar trend in the number of PMΦs that contained activated caspase-1 and underwent cell death under LPS-primed conditions (Figure 3D), as previously reported (Nyström et al., 2013).

These results further indicated that caspase-1 is activated in a digital manner. Varying the stimulus intensity or the inflammasome type did not affect the kinetics of caspase-1 activation at the single-cell level; however, at the population level, it influenced the frequency of cell death as a result of inflammasome activation.

Dying PMΦs Containing Activated Caspase-1 as the Main Source of Secreted IL-1β

Our results raised the possibility that PMΦs undergoing cell death immediately after caspase-1 activation are the main source of secreted IL-1β. Although this possibility has long been considered, single-cell studies are required to test the possibility directly and precisely, and few such investigations have been conducted because of technical limitations (Perregaux and Gabel, 1994). Our SCAT1 system allowed us to perform concurrent live imaging of caspase-1 activation, cell death, and IL-1β secretion and combine it with quantitative monitoring of IL-1β secretion in real time at single-cell resolution using a method that we recently developed (Shirasaki et al., 2014). SCAT1$^+$ PMΦs seeded on a microwell device were used to measure caspase-1 activation and IL-1β secretion at single-cell resolution on total internal reflection fluorescent microscopy. After stimulation with poly(dA:dT), the cellular activity of caspase-1 and subsequent IL-1β release from single cells were successfully detected (Figure 4A; Movie S4). IL-1β was secreted in massive amounts immediately after caspase-1 activation, and we therefore called this release an IL-1β burst. Notably, the IL-1β burst coincided with the time of cell death, which was indicated by

Figure 1. Real-Time Detection of Caspase-1 Activation through the NLRP3 Inflammasome with SCAT1, a Genetically Encoded Probe for Monitoring Caspase-1 Activation

(A) Schematic representation of SCAT1, a fluorescence resonance energy transfer biosensor developed for monitoring caspases activation. Right, linker sequences of SCAT3 (caspase-3 cleavage site DEVD) and SCAT1 (caspase-1 cleavage site YVAD).

(B and C) Live-imaging analysis of SCAT1$^+$ macrophages (PMΦs) primed with lipopolysaccharide (LPS) and stimulated with silica. Top, SCAT1 Venus/ECFP (V/C) ratio images of PMΦs treated with LPS (1 μg/ml) + silica (0.5 mg/ml) and LPS (1 μg/ml) + silica (0.5 mg/ml) + YVAD (50 μM). Bottom, time course of relative intensities of ECFP and Venus or SCAT1 V/C ratio changes of PMΦs indicated by arrowheads. The percentages of cells in a field that showed reduced SCAT1 V/C ratio are presented as means and standard deviation (SD) (C). YVAD: z-YVAD-fmk, caspase-1 inhibitor. Scale bar, 50 μm; arrowhead: representative cell. Data are representative of three or more independent experiments in (B); $n > 4$ under each condition, and $^{***}p < 0.001$ (one-way analysis of variance [ANOVA]) in (C).

(D) Live-imaging analysis of TO-PRO-3 staining of SCAT1$^+$ PMΦs under the LPS + silica stimulation condition. Left, time-lapse images of SCAT1 V/C ratio, ECFP, and TO-PRO-3 uptake. Right, time-course of SCAT1 V/C-ratio change and TO-PRO-3 uptake in the PMΦ. Scale bar, 50 μm. Data are representative of three independent experiments.

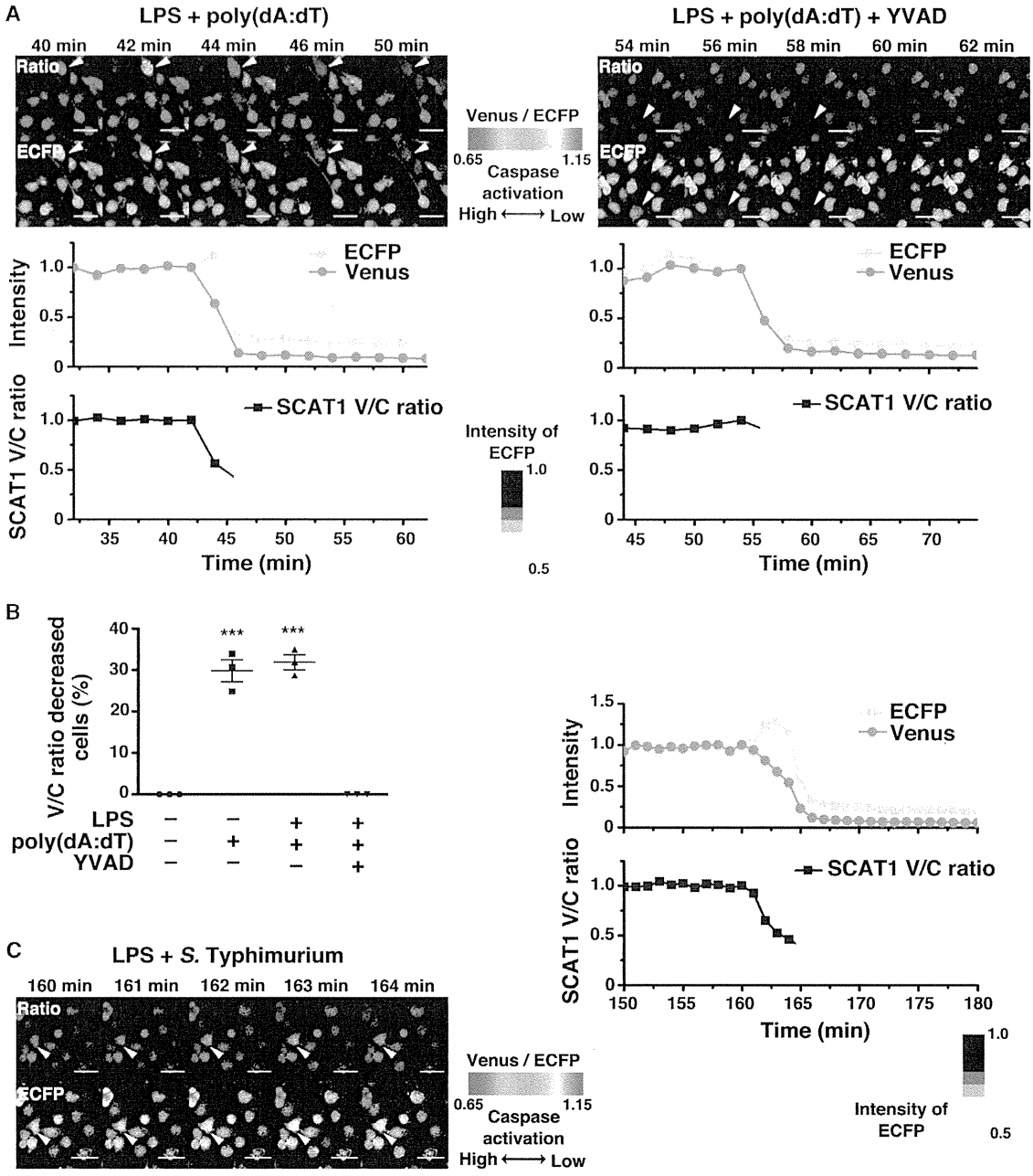

Figure 2. Real-Time Detection of Caspase-1 Activation through the AIM2 and NLRC4 Inflammasomes

(A and B) Live-imaging analysis of SCAT1$^+$ PMΦs under AIM2 inflammasome activation. Top, SCAT1 V/C ratio changes of SCAT1$^+$ PMΦs transfected with LPS (1 μg/ml) + poly(dA:dT) (1 μg/ml) and LPS (1 μg/ml) + poly(dA:dT) (1 μg/ml) + YVAD (50 μM). Bottom, time course of changes in the relative intensity of ECFP and Venus or SCAT1 V/C ratios of PMΦs indicated by arrowheads. The percentages of cells in a field that showed a reduction in the SCAT1 V/C ratio are presented as means and SD (B). Scale bar, 50 μm; arrowhead: representative cell. Data are representative of three independent experiments in (A); n > 3 under each condition, ***p < 0.001 (one-way ANOVA) in (B).

(C) Live-imaging analysis of SCAT1$^+$ PMΦs under NLRC4 activation. Left, SCAT1 V/C ratio images of PMΦs primed with LPS (1 μg/ml) and infected with *Salmonella* Typhimurium (MOI 20). Right, time course of changes in the relative intensities of ECFP and Venus or SCAT1 V/C ratios of the PMΦs indicated by arrowheads. Scale bar, 50 μm; arrowhead: representative cell. Data are representative of three independent experiments.

the disappearance of SCAT1 fluorescence (52 min in Figures 4A and 4B). To investigate whether all the cells that exhibited the IL-1β burst died, we examined the relationship between the IL-1β signal and cell death. Our results indicated that the cells that secreted IL-1β also died and that no surviving cells secreted IL-1β under this condition (Figure 4C). Furthermore, inhibiting caspase-1 activation did not inhibit cell death but prevented IL-1β release (Figure 4C). These results clearly demonstrated

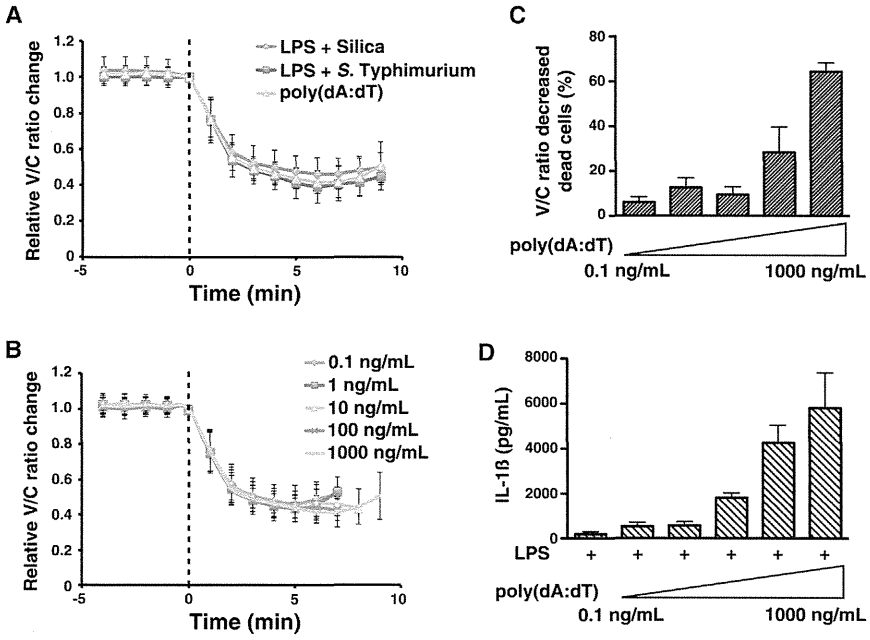

Figure 3. Almost Identical Kinetics of Caspase-1 Activation and Resulting Inflammatory Cell Death Induced by Distinct Stimuli

(A and B) Relative SCAT1 V/C ratio changes before and after caspase-1 activation. PMΦs were stimulated with distinct inflammasome activators (NLRP3: LPS [1 μg/ml] + silica [0.5 mg/ml], NLRC4: LPS [1 μg/ml] + *S.* Typhimurium [MOI 20], and AIM2: poly[dA:dT] [1 μg/ml]) (A) or transfected with poly(dA:dT) (0.1, 1, 10, 100, and 1,000 ng/ml) (B) and then examined live for 4 hr. Numbers of cells (n) used for quantifying SCAT1 V/C ratios under various conditions were (A) 32 for LPS + silica, 26 for LPS + *S.* Typhimurium, and 115 for poly(dA:dT). For poly(dA:dT) in (B), n = 42 (0.1 ng/ml), 78 (1 ng/ml), 64 (10 ng/ml), 88 (100 ng/ml), and 119 (1,000 ng/ml). x axis, time (min). Data were collected from two or more independent experiments and are presented as mean and SD.

(C) Percentages of PMΦs that contained activated caspase-1 and died, as determined based on the loss of fluorescence in all cells examined under the microscope. PMΦs were transfected with poly(dA:dT) (0.1, 1, 10, 100, and 1,000 ng/ml) and imaged live for 3 hr. Data were collected from four independent experiments and are presented as mean and SD.

(D) ELISA performed on interleukin (IL)-1β that was secreted into cell culture supernatants from SCAT1$^+$ PMΦs. The PMΦs were primed with LPS (1 μg/ml) for 4 hr and transfected with poly(dA:dT) (0.1, 1, 10, 100, 1000 ng/ml) for 3 hr. Data were collected from four independent experiments and are presented as mean and SD.

that inflammasome-mediated digital activation of caspase-1 couples the IL-1β burst with cell death and that dying cells containing activated caspase-1 are the main source of secreted IL-1β in PMΦ populations.

DISCUSSION

This study, which used a probe designed to detect caspase-1 activation, showed that caspase-1 activation is an all-or-none response at the single-cell level in PMΦs. It also demonstrated that the kinetics of caspase-1 is essentially the same irrespective of the intensity or types of stimulus. The output of caspase-1 activation is a burst of IL-1β release, which also occurs in an all-or-none manner as a consequence of digital activation of caspase-1. However, the mechanisms underlying these digital, all-or-none responses remain unclear. The assembly of large oligomeric signalosomes containing members of the Toll-like receptor interleukin-1 receptor superfamily has been suggested to be a structural basis for a digital all-or-none response (Ferrao et al., 2012; Wu, 2013). As well, such higher-order signalosomes have recently been reported to exist in inflammasomes (Lu et al., 2014), which may be the mechanism that dictates the digital activation of caspase-1.

Caspase-1 activation has long been considered to induce IL-1β secretion and cell death, and IL-1β secretion is correlated with cell death (Brough and Rothwell, 2007; Hogquist et al., 1991; Nyström et al., 2013). However, whether individual cells that contain activated caspase-1 secrete IL-1β and die has remained unclear because the investigative methods available to date have been bulk assays, which cannot address these questions. Recently, two biosensors that monitor caspase-1 and inflammasome activation were reported: a bioluminescence resonance energy transfer sensor to detect pro-IL-1β processing and a sensor fusion protein of luciferase and pro-IL-1β (Bartok et al., 2013; Compan et al., 2012). Such luminescence-based probes are superior to fluorescent probes in that they allow examination of bulk activity in cell populations or at the tissue level; however, the cellular resolution and sensitivity of these probes are insufficient for single-cell analysis within tissues. Furthermore, these sensors appear inadequate from a time-resolution standpoint for determining the kinetics of rapid caspase-1 activation within a single cell. By comparison, the indicator we developed, SCAT1, enables visualization of caspase-1 activation and measurement of its kinetics at high temporal resolution on the single-cell level. Although we do not exclude the possibility that our SCAT1 and IL-1β imaging are insensitive to weak or local activations of caspase-1 and very low amounts of IL-1β secretion, previous bulk assays including western blotting and ELISA are less sensitive than our single-cell imaging system and almost impossible to use to test this possibility. Addressing these issues requires further technical developments.

Elevated local or systemic IL-1β release caused by compromised inflammasome activation is associated with various chronic inflammatory diseases such as cryopyrin-associated periodic syndrome, metabolic disorders, and carcinogenesis in human and mouse models (Wen et al., 2012; Zitvogel et al., 2012). Recently, mutations in an NLRP3 protein associated with cryopyrin-associated periodic syndrome were shown to induce necrotic cell death, which in turn leads to neutrophilic inflammation (Satoh et al., 2013). Our study clearly demonstrates that dying MΦs containing activated caspase-1 exhibit IL-1β bursts. Thus, cells located near such MΦs would receive a maximal level

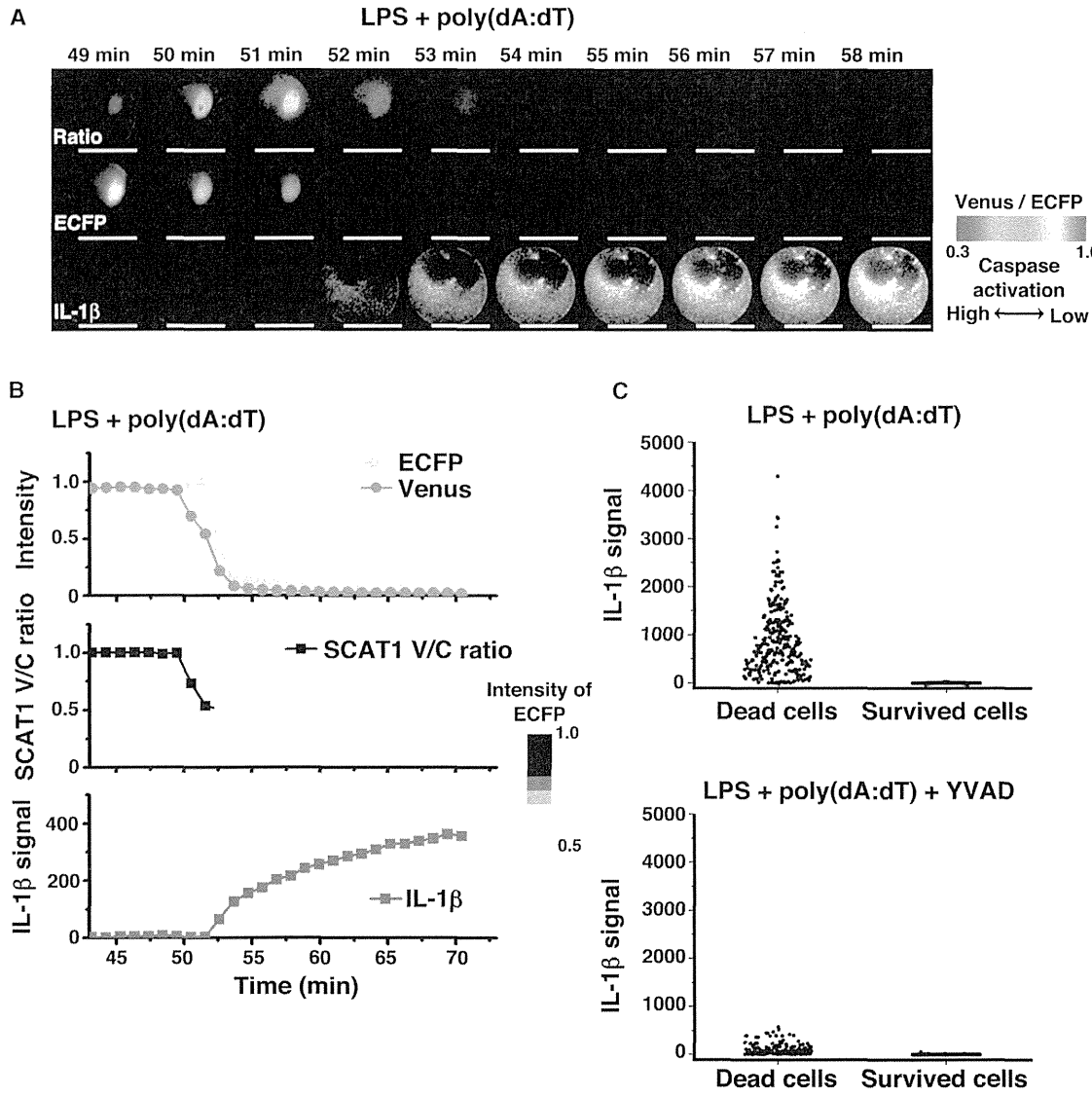

Figure 4. Dying PMΦs Containing Activated Caspase-1 as the Main Source of Secreted IL-1β

(A and B) Simultaneous live imaging of SCAT1 V/C-ratio changes and IL-1β secretion in SCAT1$^+$ PMΦs primed using LPS (1 μg/ml) and stimulated with poly(dA:dT) (1 μg/ml). (A) The montage shows time-dependent changes in the intensities of ECFP (the middle row), SCAT1 V/C ratios (the top row), and IL-1β secretion (the bottom row). (B) The time course of changes in the intensities of ECFP and Venus, SCAT1 V/C ratios, and IL-1β secretion in a representative cell, as in (A). Scale bar, 50 μm.

(C) Dot-plot representation of the signal intensity of IL-1β secreted from single cells, classified according to cell viability in the absence and presence of treatment with the caspase-1 inhibitor YVAD. LPS-primed SCAT1$^+$ PMΦs were introduced into a microwell array with a fluorescent detection antibody and stimulated with poly(dA:dT). After incubation for 4 hr, all microwells were scanned to detect the signals of IL-1β secretion and the SCAT1 probe. Cell viability was determined based on the intensity of SCAT1.

of IL-1β locally, even when a low level of circulating IL-1β is detected systemically. This scenario is highly likely to occur under chronic disease conditions. If the local cells receiving the burst-released IL-1β exhibit oncogenic potential, strong stimulation by high levels of IL-1β could trigger cellular transformation under conditions of chronic inflammation. Studies of inflammatory cell death and local bursts of cytokine release in vivo could offer intriguing and crucial perspectives that will help reveal the mechanisms underlying chronic inflammatory diseases. Applying SCAT1 imaging analysis to various chronic inflammatory disease models in vivo is challenging but would enhance our understanding of the involvement of local and continuous inflammatory cell death in the pathology of these diseases.

EXPERIMENTAL PROCEDURES

Live Imaging of Peritoneal MΦ Cultures

Live imaging was conducted using an inverted confocal microscope (TCS SP5; Leica) equipped with a galvo stage and a resonant scanner designed for fast scanning using an HC PL APO 20×/0.70 CS dry objective (Leica).

During imaging, dishes of cells were placed in a humidified cell-culture incubator and continuously supplied with 5% CO_2/air at 37°C (Tokai Hit Company). ECFP was excited using a 442 nm diode laser (10%–25% power), and the emissions of ECFP and Venus (FRET) were detected simultaneously using two detectors (Leica HyD) and a resonant scanner (8,000 Hz; Leica). Propidium iodide and TO-PRO-3 were excited using 561 and 633 nm diode lasers (15% power), respectively. Images (512 × 512 pixels) were acquired at intervals of 1–2 min, and the z slices obtained were 4 μm thick (total of 9–12 slices/time point), depending on the experiment. To inhibit caspase-1 pharmacologically, we used z-YVAD-fmk (50 μM final concentration; 1/1,000 dilution of a 50 mM stock prepared in dimethylsulfoxide).

PMΦs were plated on four-well glass-bottom dishes (Greiner Bio-One) and primed using LPS (1 μg/ml) or PBS for 4–12 hr before stimulation. All live-imaging analyses were initiated after stimulating inflammasomes by using this procedure, and live images were acquired for 3–4 hr under all conditions tested.

SUPPLEMENTAL INFORMATION

Supplemental Information includes Supplemental Experimental Procedures, four figures, and four movies and can be found with this article online at http://dx.doi.org/10.1016/j.celrep.2014.07.012.

AUTHOR CONTRIBUTIONS

T.L., Y.Y., and M.M. designed the study; T.L., Y.S., K.S., and Y.Y. performed most of the experiments and data analysis; Y.S. and M.Y. performed the single-cell live imaging of cytokine secretion and data analysis; K.H., T.K., K.T., T.S., E.K., and O.O. provided essential advice and resources; and T.L., Y.Y., and M.M. prepared the manuscript.

ACKNOWLEDGMENTS

We are grateful to K. Kuida (Millennium: The Takeda Oncology Company), R. Uchiyama, and H. Tsutsui (Hyogo College of Medicine, Japan) for providing caspase-1/11-deficient mice, M. Okabe (Osaka University) for providing CAG-Cre mice (Riken BRC), and Y. Sasaki (Kyoto University) for providing the Rosa26-CAG-STOP targeting vector. We thank the University of Tokyo and Leica Microsystems Imaging Center for the imaging analysis. We also thank N. Kambe (Chiba University), T. Chihara, and all the members of the M.M. laboratory for the helpful discussions and comments and M. Sasaki, K. Tomioka, Y. Fujioka, T. Takahashi, and Y. Watanabe for experimental assistance. This work was supported by grants to M.M. and Y.Y. from the Ministry of Education, Culture, Sports, Science and Technology in Japan, the Japan Society for the Promotion of Science, and the Japan Science and Technology Agency.

Received: December 27, 2013
Revised: May 26, 2014
Accepted: July 13, 2014
Published: August 7, 2014

REFERENCES

Aoki, K., Kamioka, Y., and Matsuda, M. (2013). Fluorescence resonance energy transfer imaging of cell signaling from in vitro to in vivo: basis of biosensor construction, live imaging, and image processing. Dev. Growth Differ. *55*, 515–522.

Bartok, E., Bauernfeind, F., Khaminets, M.G., Jakobs, C., Monks, B., Fitzgerald, K.A., Latz, E., and Hornung, V. (2013). iGLuc: a luciferase-based inflammasome and protease activity reporter. Nat. Methods *10*, 147–154.

Brough, D., and Rothwell, N.J. (2007). Caspase-1-dependent processing of pro-interleukin-1beta is cytosolic and precedes cell death. J. Cell Sci. *120*, 772–781.

Broz, P., von Moltke, J., Jones, J.W., Vance, R.E., and Monack, D.M. (2010). Differential requirement for Caspase-1 autoproteolysis in pathogen-induced cell death and cytokine processing. Cell Host Microbe *8*, 471–483.

Compan, V., Baroja-Mazo, A., Bragg, L., Verkhratsky, A., Perroy, J., and Pelegrin, P. (2012). A genetically encoded IL-1β bioluminescence resonance energy transfer sensor to monitor inflammasome activity. J. Immunol. *189*, 2131–2137.

Denes, A., Lopez-Castejon, G., and Brough, D. (2012). Caspase-1: is IL-1 just the tip of the ICEberg? Cell Death Dis. *3*, e338.

Fernandes-Alnemri, T., Yu, J.W., Datta, P., Wu, J., and Alnemri, E.S. (2009). AIM2 activates the inflammasome and cell death in response to cytoplasmic DNA. Nature *458*, 509–513.

Ferrao, R., Li, J., Bergamin, E., and Wu, H. (2012). Structural insights into the assembly of large oligomeric signalosomes in the Toll-like receptor-interleukin-1 receptor superfamily. Sci. Signal. *5*, re3.

Fink, S.L., and Cookson, B.T. (2005). Apoptosis, pyroptosis, and necrosis: mechanistic description of dead and dying eukaryotic cells. Infect. Immun. *73*, 1907–1916.

Franchi, L., Muñoz-Planillo, R., and Núñez, G. (2012). Sensing and reacting to microbes through the inflammasomes. Nat. Immunol. *13*, 325–332.

Hogquist, K.A., Nett, M.A., Unanue, E.R., and Chaplin, D.D. (1991). Interleukin 1 is processed and released during apoptosis. Proc. Natl. Acad. Sci. USA *88*, 8485–8489.

Hornung, V., Ablasser, A., Charrel-Dennis, M., Bauernfeind, F., Horvath, G., Caffrey, D.R., Latz, E., and Fitzgerald, K.A. (2009). AIM2 recognizes cytosolic dsDNA and forms a caspase-1-activating inflammasome with ASC. Nature *458*, 514–518.

Kayagaki, N., Warming, S., Lamkanfi, M., Vande Walle, L., Louie, S., Dong, J., Newton, K., Qu, Y., Liu, J., Heldens, S., et al. (2011). Non-canonical inflammasome activation targets caspase-11. Nature *479*, 117–121.

Keller, M., Rüegg, A., Werner, S., and Beer, H.D. (2008). Active caspase-1 is a regulator of unconventional protein secretion. Cell *132*, 818–831.

Kuida, K., Lippke, J.A., Ku, G., Harding, M.W., Livingston, D.J., Su, M.S., and Flavell, R.A. (1995). Altered cytokine export and apoptosis in mice deficient in interleukin-1 beta converting enzyme. Science *267*, 2000–2003.

Kuranaga, E., Matsunuma, T., Kanuka, H., Takemoto, K., Koto, A., Kimura, K., and Miura, M. (2011). Apoptosis controls the speed of looping morphogenesis in Drosophila male terminalia. Development *138*, 1493–1499.

Latz, E., Xiao, T.S., and Stutz, A. (2013). Activation and regulation of the inflammasomes. Nat. Rev. Immunol. *13*, 397–411.

Lu, A., Magupalli, V.G., Ruan, J., Yin, Q., Atianand, M.K., Vos, M.R., Schröder, G.F., Fitzgerald, K.A., Wu, H., and Egelman, E.H. (2014). Unified polymerization mechanism for the assembly of ASC-dependent inflammasomes. Cell *156*, 1193–1206.

Martinon, F., Burns, K., and Tschopp, J. (2002). The inflammasome: a molecular platform triggering activation of inflammatory caspases and processing of proIL-beta. Mol. Cell *10*, 417–426.

Miao, E.A., Leaf, I.A., Treuting, P.M., Mao, D.P., Dors, M., Sarkar, A., Warren, S.E., Wewers, M.D., and Aderem, A. (2010). Caspase-1-induced pyroptosis is an innate immune effector mechanism against intracellular bacteria. Nat. Immunol. *11*, 1136–1142.

Miura, M., Zhu, H., Rotello, R., Hartwieg, E.A., and Yuan, J. (1993). Induction of apoptosis in fibroblasts by IL-1 beta-converting enzyme, a mammalian homolog of the C. elegans cell death gene ced-3. Cell *75*, 653–660.

Mosser, D.M., and Edwards, J.P. (2008). Exploring the full spectrum of macrophage activation. Nat. Rev. Immunol. *8*, 958–969.

Nakajima, Y., Kuranaga, E., Sugimura, K., Miyawaki, A., and Miura, M. (2011). Nonautonomous apoptosis is triggered by local cell cycle progression during epithelial replacement in Drosophila. Mol. Cell. Biol. *31*, 2499–2512.

Nyström, S., Antoine, D.J., Lundbäck, P., Lock, J.G., Nita, A.F., Högstrand, K., Grandien, A., Erlandsson-Harris, H., Andersson, U., and Applequist, S.E. (2013). TLR activation regulates damage-associated molecular pattern isoforms released during pyroptosis. EMBO J. *32*, 86–99.

Perregaux, D., and Gabel, C.A. (1994). Interleukin-1 beta maturation and release in response to ATP and nigericin. Evidence that potassium depletion

mediated by these agents is a necessary and common feature of their activity. J. Biol. Chem. *269*, 15195–15203.

Pierini, R., Juruj, C., Perret, M., Jones, C.L., Mangeot, P., Weiss, D.S., and Henry, T. (2012). AIM2/ASC triggers caspase-8-dependent apoptosis in Francisella-infected caspase-1-deficient macrophages. Cell Death Differ. *19*, 1709–1721.

Rathinam, V.A., Vanaja, S.K., and Fitzgerald, K.A. (2012). Regulation of inflammasome signaling. Nat. Immunol. *13*, 333–342.

Satoh, T., Kambe, N., and Matsue, H. (2013). NLRP3 activation induces ASC-dependent programmed necrotic cell death, which leads to neutrophilic inflammation. Cell Death Dis. *4*, e644.

Schroder, K., and Tschopp, J. (2010). The inflammasomes. Cell *140*, 821–832.

Shirasaki, Y., Yamagishi, M., Suzuki, N., Izawa, K., Nakahara, A., Mizuno, J., Shoji, S., Heike, T., Harada, Y., Nishikomori, R., and Ohara, O. (2014). Real-time single-cell imaging of protein secretion. Sci Rep *4*, 4736.

Takemoto, K., Nagai, T., Miyawaki, A., and Miura, M. (2003). Spatio-temporal activation of caspase revealed by indicator that is insensitive to environmental effects. J. Cell Biol. *160*, 235–243.

Takemoto, K., Kuranaga, E., Tonoki, A., Nagai, T., Miyawaki, A., and Miura, M. (2007). Local initiation of caspase activation in Drosophila salivary gland programmed cell death in vivo. Proc. Natl. Acad. Sci. USA *104*, 13367–13372.

Tay, S., Hughey, J.J., Lee, T.K., Lipniacki, T., Quake, S.R., and Covert, M.W. (2010). Single-cell NF-kappaB dynamics reveal digital activation and analogue information processing. Nature *466*, 267–271.

Walsh, J.G., Logue, S.E., Lüthi, A.U., and Martin, S.J. (2011). Caspase-1 promiscuity is counterbalanced by rapid inactivation of processed enzyme. J. Biol. Chem. *286*, 32513–32524.

Wen, H., Ting, J.P., and O'Neill, L.A. (2012). A role for the NLRP3 inflammasome in metabolic diseases—did Warburg miss inflammation? Nat. Immunol. *13*, 352–357.

Wu, H. (2013). Higher-order assemblies in a new paradigm of signal transduction. Cell *153*, 287–292.

Yamaguchi, Y., Shinotsuka, N., Nonomura, K., Takemoto, K., Kuida, K., Yosida, H., and Miura, M. (2011). Live imaging of apoptosis in a novel transgenic mouse highlights its role in neural tube closure. J. Cell Biol. *195*, 1047–1060.

Zitvogel, L., Kepp, O., Galluzzi, L., and Kroemer, G. (2012). Inflammasomes in carcinogenesis and anticancer immune responses. Nat. Immunol. *13*, 343–351.

SCIENTIFIC REPORTS

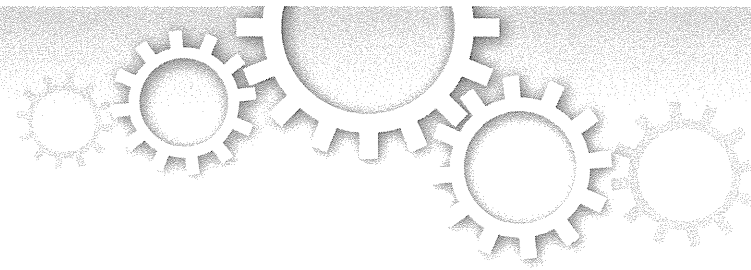

OPEN

SUBJECT AREAS:
CELL DEATH AND IMMUNE RESPONSE
LAB-ON-A-CHIP
SINGLE-CELL IMAGING
CELLULAR IMAGING

Received
3 October 2013

Accepted
2 April 2014

Published
22 April 2014

Correspondence and requests for materials should be addressed to O.O. (oosamu@rcai.riken.jp)

Real-time single-cell imaging of protein secretion

Yoshitaka Shirasaki[1], Mai Yamagishi[1], Nobutake Suzuki[1], Kazushi Izawa[2], Asahi Nakahara[3], Jun Mizuno[3], Shuichi Shoji[3], Toshio Heike[2], Yoshie Harada[4], Ryuta Nishikomori[2] & Osamu Ohara[1,5]

[1]RIKEN Center for Integrative Medical Sciences (IMS-RCAI), 1-7-22 Suehiro-cho Tsurumi-ku, Yokohama, Kanagawa 230-0045, Japan, [2]Department of Pediatrics, Kyoto University Graduate School of Medicine, 54 Shogoin-Kawahara-cho Sakyo-ku, Kyoto 606-8507, Japan, [3]Faculty of Science and Engineering, Waseda University, Okubo 3-4-1, Shinjuku, Tokyo 169-8555, Japan, [4]Institute for Integrated Cell-Material Sciences (WPI-iCeMS), Kyoto University Graduate School of Biostudies, Yoshida-Honmachi, Sakyo-ku, Kyoto 606-8501, Japan, [5]Department of Human Genome Research, Kazusa DNA Research Institute, 2-6-7 Kazusa-Kamatari, Kisarazu, Chiba 292-0818, Japan.

Protein secretion, a key intercellular event for transducing cellular signals, is thought to be strictly regulated. However, secretion dynamics at the single-cell level have not yet been clarified because intercellular heterogeneity results in an averaging response from the bulk cell population. To address this issue, we developed a novel assay platform for real-time imaging of protein secretion at single-cell resolution by a sandwich immunoassay monitored by total internal reflection microscopy in sub-nanolitre-sized microwell arrays. Real-time secretion imaging on the platform at 1-min time intervals allowed successful detection of the heterogeneous onset time of nonclassical IL-1β secretion from monocytes after external stimulation. The platform also helped in elucidating the chronological relationship between loss of membrane integrity and IL-1β secretion. The study results indicate that this unique monitoring platform will serve as a new and powerful tool for analysing protein secretion dynamics with simultaneous monitoring of intracellular events by live-cell imaging.

Many secreted proteins have been identified as important functional mediators of intercellular communication for the purpose of initiating various cellular processes, including differentiation and migration[1–3]. Cytokines in particular are one of the best studied classes of secreted proteins with broad effects on immune responses[4]. For the proper functioning of the immune system, cytokine synthesis and secretion must be tightly regulated, both spatially and temporally[5]. However, recent investigations using single-cell analysis have shown that immune cells display highly heterogeneous levels of cytokine secretion, even in cells with apparently similar phenotypes[6]. Therefore, the relationship between heterogeneous cytokine secretion at the single-cell level and the maintenance of homeostasis of the immune system has become a primary subject of investigation in the field of immunology. To address this issue, a methodology is required that enables delineation of spatiotemporal heterogeneity of cytokine secretion at the single-cell level. We have particularly focused on cytokine induction processes that occur in single cells induced by external stimulation, specifically with regard to (1) cellular heterogeneity in protein secretion dynamics and (2) the chronological relationship between intracellular event(s) and protein secretion. However, the technology available for monitoring protein secretion from single cells remains in its infancy.

Several groups have reported population analysis of cytokine secretion from single cells by using antibody-based immunoassay applications. Love *et al.* generated a secretion profile for a large collection of single cells by using microengraving[7] and succeeded in measuring the time course of cytokine secretion during T-lymphocyte maturation every 2 h for a period spanning several hours[8]. While these methods are efficient for their high throughput and/or the quantitative data generated, several challenges remain because of their inherent measurement limitations. In these methods, the accumulated cytokine molecules situated on a solid surface are labelled with a detection probe and are quantified after intensive wash steps, which are required to remove excess probe. Although this wash step, known as bound/free (B/F) separation, determines the signal/noise ratio for detection, this step also causes a lag between secretion and detection. Therefore, these methods cannot currently offer either a time interval of shorter than a few hours nor simultaneous real-time monitoring of a second intracellular variable (e.g. cell viability) over time.

Previously, our group and Salehi-Reyhani *et al.* respectively have successfully addressed this B/F separation issue in fluorescence immunoassays (FIAs) by taking advantage of near-field excitation in total internal reflection

fluorescence microscopy (TIRFM)[9,10]. In these studies, target proteins in each single-cell lysate segmented by microwells were quantified by detecting formation of immunocomplexes on the microwell bottom. In the current study, we have developed a novel assay platform for real-time monitoring of live single-cell cytokine secretion (Fig. 1). Each single cell is deposited on a microfabricated-well array (MWA) chip, which restricts cell migration as well as compartmentalizes the secretory signals from individual cells. The anti-cytokine capture antibody immobilized on the microwell bottom immediately captures the cytokine secreted from a cell, which enables TIRFM-FIA to function *in situ*. An MWA chip of the platform has an open architecture at the top of each microwell to permit easy access for stimulus delivery and to maintain culture conditions similar to those of a bulk experiment.

We characterized our secretion assay platform using a MWA chip consisting of glass and polydimethylsiloxiane (PDMS) in a quantitative manner by model experiments, introducing minute amounts of cytokine into microwells to mimic the milieu of cytokine secretion from a single cell. The platform was applied to monitor cytokine secretion from human peripheral blood monocytes at 1-min time intervals. We examined the IL-1β secretion process while simultaneously observing membrane integrity to determine the intracellular processes that occur at the time of cytokine secretion, since the mechanism underlying the non-classical IL-1β secretion pathway currently remains unclear.

Results

Characterization of an assay platform for real-time secretion imaging in an MWA chip. In this study, we designed a real-time single-cell imaging platform to monitor the secretion processes over time. We fabricated a novel MWA chip consisting of a PDMS well wall and a glass well bottom (see Supplementary Fig. S1a online). An objective of numerical aperture 1.49 was used to avoid the stray light due to the higher refractive index of PDMS (n = 1.42, Sylgard®184, Dow Corning Co., http://www1.dowcorning.com/DataFiles/090007c8803bb6a1.pdf) than that of medium (n = 1.34; Supplementary Fig. S1b–d). To assess restriction of the horizontal movement of secreted cytokine molecules by the microwell structure, we compared the decrease of fluorescently labelled protein from an observation area for TIRFM with and without microwell structures. The microwell structure slowed the escape of fluorescent molecules by about 20-fold (see Supplementary Fig. S2).

Next, to assess the functionality of time-resolved FIA (even in the open MWA), we introduced a miniscule amount of cytokine into microwells by using a microinjector to mimic cytokine secretion from a single cell (Fig. 2a). Fluorescence signals began to increase immediately after pulsed injection of IL-1β (time = 0; Fig. 2b, c) and increased without apparent change in localization over time (Fig. 2b), indicating that most of the injected IL-1β was instantly captured by antibody on the MWA bottom before diffusion throughout the microwell. From a separate experiment, we found that the fluorescence signals after the injection of pre-formed IL-1β-detection antibody complexes increased 15 times faster than that after the injection of IL-1β alone, suggesting that the released IL-1β rapidly bound to the capture antibodies on the bottom surface of the MWA chip (Fig. S3a, b). Therefore, binding of the detection antibody to form sandwich immunocomplexes was likely the rate-limiting step for the increase in the fluorescence signals under the experimental conditions employed. Once the immunocomplex was formed, its dissociation occurred very slowly (dissociation constant $k_{off} < 2 \times 10^{-6}$ s^{-1}, Fig. S3c).

The rising curves of the fluorescence signal obtained from IL-1β injection were fitted with a single exponential, especially during

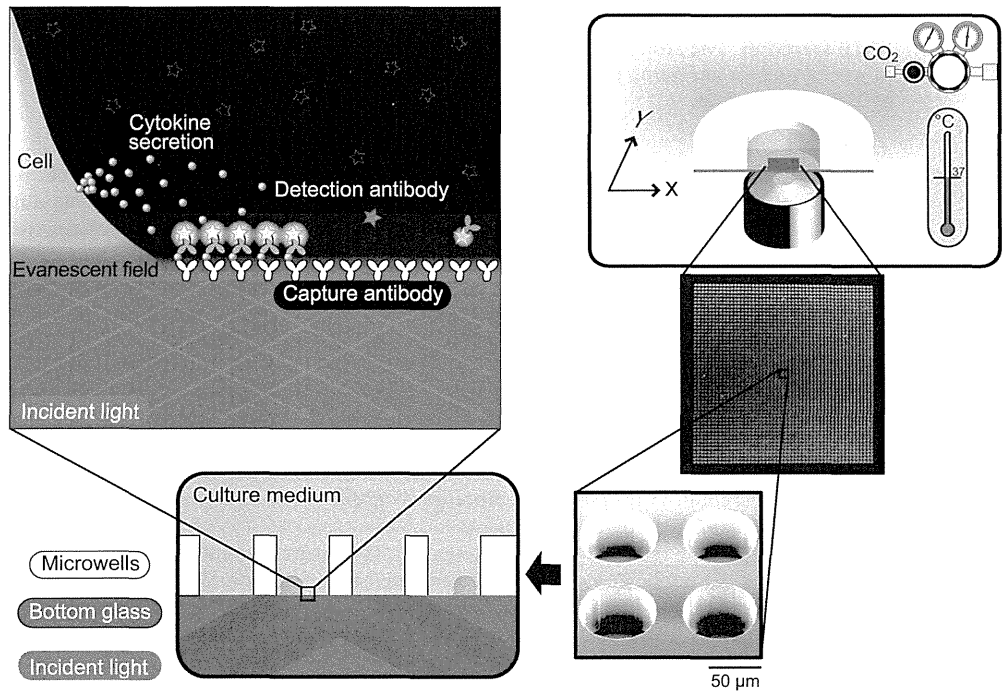

Figure 1 | Concept of the real-time single cell secretion assay platform. The schematic illustrates the concept of the platform for the real-time single cell secretion assay. The platform works with micro-fabricated well-array chip on a fully automated fluorescence microscopy. The platform maintains the environment (temperature, concentration of CO_2, and humidity) of the chip. The chip has an array of nanolitre-sized microwells with a glass bottom, into which individual cells were introduced separately. The well has open-ended structure; therefore, culture medium was exchanged constantly during the observation. The anti-cytokine capture antibody was immobilized on the well bottom, onto which secreted cytokine and fluorescently labelled detection antibody were bound to form a sandwich immunocomplex. Near-field excitation by total internal reflection enabled selective detection of the cytokine sandwich immunocomplex immediately following secretion without the requirement for wash steps.

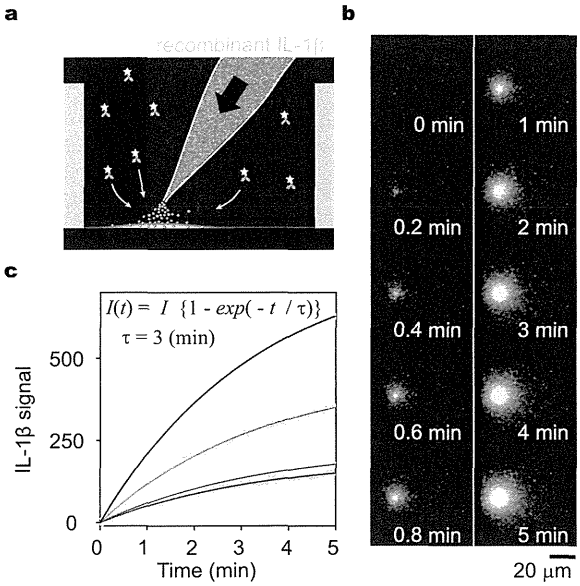

Figure 2 | Performance evaluation of time-resolved FIA in the MWA on model experiments using a microinjector. (a) Schema of the model experiment using pulsed injection of IL-1β via a microinjector. An increase in fluorescence signal was observed after pulse injecting 100 ng/mL of recombinant IL-1β into a microwell that was filled with the detection medium containing 30 nM fluorescently labelled detection antibody. (b) Representative images of developing fluorescence signals obtained from time-resolved FIA after introducing recombinant IL-1β into the microwell. Images were acquired once every second applying a 60-ms exposure time. The time elapsed after the pulsed injection is shown on each image. (c) Time course of the average intensity of the IL-1β signal in a microwell. Each dot denotes a measured value and solid lines denote fitted curves. Different colours denote different durations under a constant pressure of injection (1,200 Pa): 4 s (black), 2 s (green), 0.5 s (blue), and 0.1 s (cyan). Curve fitting was performed for every dataset from 0 to 5 min using the global parameter of time constant, τ, and local parameters of maximum intensity, I, and consequently τ was determined as 3 min.

5 min after injection, and the time constant was estimated to be 3 min (Fig. 2c). Using this parameter, we evaluated the accuracy for determination of the onset time by fitting a single exponential to the dataset quantifying the fluorescence increase obtained within an arbitrary time interval. The accuracy of computed onset time was determined within 0.1 min when using a dataset with 1-min time intervals (Fig. S4).

The increase in the amount of fluorescence signal depended upon the quantity of IL-1β injected (Fig. 2c). However, the absolute amount of secreted cytokine could not be determined because of the difficulties in controlling the local concentration of cytokines within an open-ended microwell to generate a standard curve. Additionally, immobilized cytokine captured by antibody on the MWA surface was considered to be part of the overall secreted cytokine, while the non-immobilized fraction diffused into the medium. The captured ratio would depend upon an uncontrollable variable, such as the height of the cytokine release point (which determines the probability of the cytokine encountering the capture antibody). Therefore, the assay platform developed in this study was best suited for detection of the onset of secretory molecule secretion from single cells at high time resolution (probably less than 1 min) while also providing semi-quantitative data on secreted molecules. In experiments performed using microwells closed with sealing oil, the platform could detect the signal from 2,000 molecules of IL-1β in a microwell (Supplementary Fig. S5).

Real-time monitoring of IL-6 secretion from single living monocytes within a 1-min time interval. As a proof-of-concept experiment, we assessed the performance of our assay platform for time-resolved observation using lipopolysaccharide (LPS)-stimulated human peripheral blood monocytes by simultaneous detection of cytokine secretion and live/dead signals. We confirmed that proinflammatory cytokines were detected in the culture supernatant of 1×10^5 monocytes stimulated with 1 μg/mL LPS (first priming; Supplementary Fig. S6). Among the detectable cytokines, we selected interleukin 6 (IL-6) as a typical cytokine, known to be released using classical pathways involving ER/Golgi trafficking[11].

First, we examined the reactivity and viability of monocytes in the MWA from snapshot measurements of 2,500 microwells after LPS stimulation for 4 h. Of the 584 cells observed from 2,500 microwells, 23 cells displayed the IL-6 signal (4%). Calcein (+)/SYTOX (−) living cells accounted for 60% of the total cells, but 91% of IL-6–positive cells. Next, 40 microwells were scanned for 4 h for real-time IL-6 secretion imaging at 1-min time intervals. After three independent experiments, we could analyse 71 single cells, including 56 living cells; 7 individual cells were observed to secrete IL-6 (representative images are displayed in Fig. 3a and Supplementary movie 1). IL-6 signals increased gradually for over 1 h after stimulation (Fig. 3b) without change in the SYTOX signal (Fig. 3b), as observed in the displayed dead cell (Fig. 3c). All the remaining IL-6–secreting cells continued to survive during the observation period. These results demonstrated that the single-cell secretion assay platform enabled us to monitor physiological secretion of IL-6 from live monocytes.

Simultaneous imaging of extracellular IL-1β secretion and plasma membrane integrity. The mechanism underlying IL-1β secretion remains poorly understood, although it is known that IL-1β is a key mediator of inflammation[12–14]. Several researchers have proposed various mechanisms for IL-1β secretion[15,16]; however, many details remain to be validated due to a lack of techniques for monitoring real-time secretion processes of IL-1β at single-cell resolution. Therefore, we monitored IL-1β secretion from individual monocytes at high temporal resolution in parallel with observation of the cellular physiological states at the time of secretion.

In this study, monocytes were costimulated with both LPS and adenosine triphosphate (ATP), because IL-1β release from monocytes is known to require a second signal (i.e. ATP) to activate the intracellular inflammasome in addition to priming with pathogen-associated molecular stimuli (i.e. LPS)[17–19]. Glycine was added to the culture medium during stimulation because glycine blocks cytolytic release of pro–IL-1β without affecting the secretion of mature IL-1β (Supplementary Fig. S6)[15,20,21].

Before real-time monitoring, we analysed IL-1β secretion and the live/dead state by snapshot secretion measurements of single cells with calcein/SYTOX staining (Fig. 4a) in 2,500 microwells at 4 h after LPS/ATP stimulation (Supplementary Fig. S7). This snapshot measurement demonstrated that approximately 30% of single monocytes secreted IL-1β. Interestingly, 99% of these IL-1β–secreting cells lost the calcein signal and were stained with SYTOX. When lower LPS concentration (10 ng/mL) was tested, both the number of IL-1β-secreting cells and the amount of secreted IL-1β per monocytes were decreased while the percentage of dead cells was only slightly affected (Supplementary Table S1). The concomitant disappearance of calcein and the increase in SYTOX signal reflect the compromised status of the cell membrane. Therefore, these results suggested some degree of association between IL-1β secretion and the loss of cell membrane integrity, exhibiting a sharp contrast with IL-6 secretion from LPS-stimulated monocytes (in which the vast majority of IL-6 secreting cells remained calcein-positive).

We then performed real-time secretion imaging of IL-1β from monocytes, focusing on whether IL-1β secretion was preceded or followed by a loss of cellular membrane integrity. The experiments

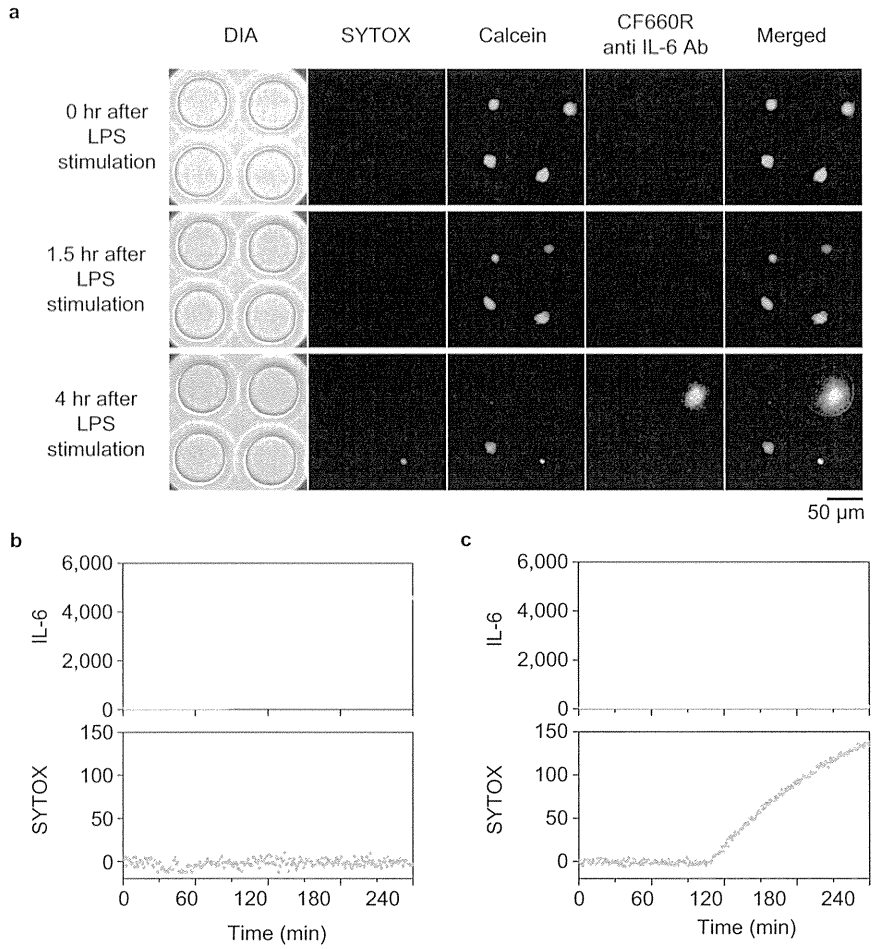

Figure 3 | Time-resolved monitoring of IL-6 secretion after a classical secretion pathway. Calcein-charged human peripheral blood monocytes were introduced into the MWA chip. Signals of SYTOX, calcein and IL-6 secretion were observed with 1-min time intervals after administration of 1 μg/mL of LPS. (a) Representative images of multichannel microscopy. Morphological features of a human monocyte were monitored under diascopic illumination (DIA). The fluorescence signal of SYTOX-stained nuclei was magenta (SYTOX), that of calcein-stained cell bodies was green (Calcein), and that of secreted IL-6 was yellow (CF660R anti IL-6 Ab). Merged images of these three fluorescence signals are also displayed (Merged). Each image was generated at the described time point. Scale bar, 50 μm. Although cells floated soon after LPS stimulation, cells began to adhere to the microwell bottom at 1.5 h after LPS stimulation, with some exhibiting the IL-6 signal at 4 h after LPS stimulation. Although the fluorescence intensity of calcein per pixel was apparently decreased due to the cell deformation, it was distinct from a sharp drop of calcein signal observed for dead cells like in the bottom-right well. The cells that underwent cell death showed elevation of the SYTOX signal. (b), (c) Time course of the average intensity of IL-6 and SYTOX signals within microwells shown in Figure 3a: the top right (b) or the bottom right (c) microwell. (b) The IL-6 secretion signal gradually increased from 80 min after LPS stimulation without any change in SYTOX signal. (c) Typical example of a dead cell. Only the SYTOX signal was increased.

were performed twice, measuring 54 individual monocytes, 20 of which secreted detectable quantities of IL-1β. While all of these cells were calcein-positive before ATP stimulation, they lost their calcein signal and subsequently stained with SYTOX, consistent with the aforementioned snapshot observations (Supplementary movie 2 and Fig. 4b). Disappearance of the calcein signal occurred rapidly and was completed within a few minutes. By contrast, the observed increases in SYTOX signalling consisted of two phases: the first occurred gradually upon ATP stimulation and the second occurred abruptly at various moments following ATP stimulation. These two phases suggest that cell membrane permeability for SYTOX influx was altered through multiple stages.

Surprisingly, IL-1β secretion appeared to coincide with calcein disappearance and the second SYTOX influx (Supplementary movie 2 and Fig. 4c). The increase in the signal of IL-1β secretion occurred as a concave-down function, suggesting IL-1β was secreted in a burst release pattern (Supplementary Fig. S8). To evaluate the association between these events, the transition times were determined by curve fitting of the equation (1), (2), or (3) to the mean fluorescence intensities over time and were compared with one another (Supplementary Fig. S9). Although the response times after ATP stimulation were quite heterogeneous among cells, the transition time of calcein disappearance, SYTOX influx, and IL-1β release were quite similar in most cells (Fig. 5a and b). By focusing on the timeline of these events, lag times between SYTOX influx or IL-1β release and calcein disappearance were calculated. The SYTOX influx and the calcein disappearance (both resulting from membrane imperfections) occurred simultaneously or nearly simultaneously, and SYTOX influx was only slightly delayed following calcein disappearance (mean, 0.2 min; Fig. 5c). By contrast, IL-1β release occurred several minutes following calcein disappearance (mean, 2.0 min, except for 2 outliers; Fig. 5d), and its lag times were more variable than those of SYTOX influx. Two outliers exhibited extremely long delays (44.5 and 105.9 min) in IL-1β release after calcein disappearance. These results indicated that burst release of IL-1β was preceded by loss of cell membrane integrity.

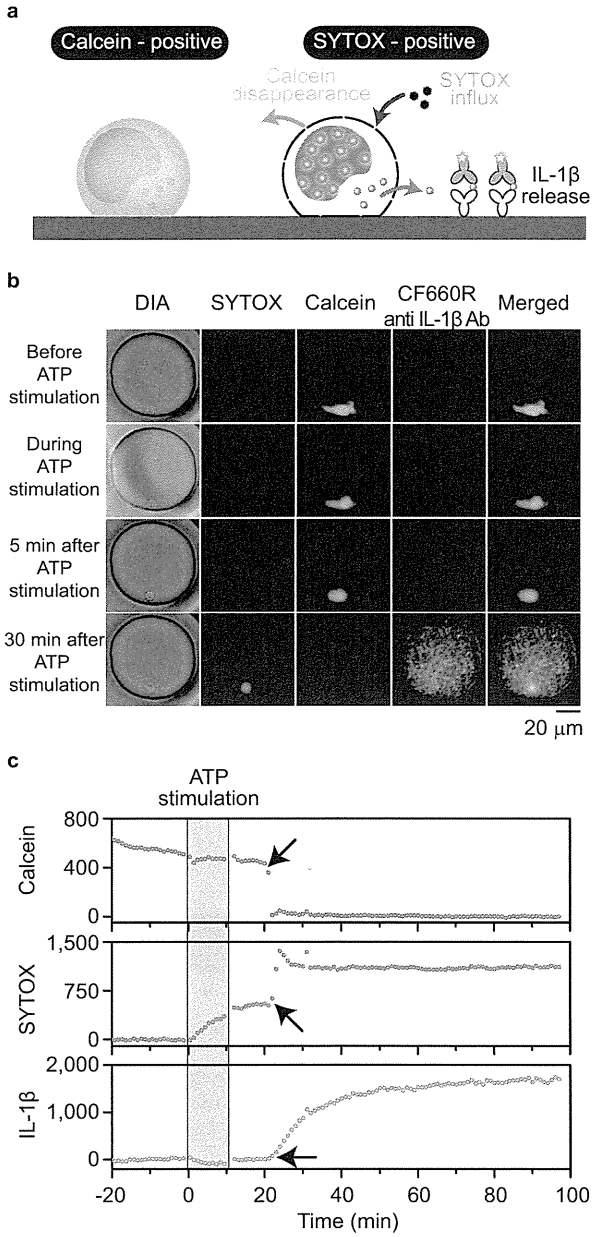

Figure 4 | Time-resolved monitoring of IL-1β secretion on the PDMS MWA chip. (a) Schematic of simultaneous monitoring of IL-1β secretion and cell membrane integrity using calcein and SYTOX staining. SYTOX influx and fluorescent calcein disappearance was observed due to compromised plasma membrane integrity. (b) Representative images of multichannel microscopy. Morphological features of a human monocyte were monitored under diascopic illumination (DIA). The fluorescence signal of SYTOX-stained nuclei was magenta (SYTOX), that of a calcein-stained cell bodies was green (Calcein), and that of secreted IL-1β was yellow (CF660R anti IL-1β Ab). Merged images of these three fluorescence signals are also displayed (Merged). Each image was obtained at the described period. Scale bar, 20 μm. (c) Example of the signal time course during time-resolved monitoring. Grey bands represent the period when the monocytes were exposed to ATP. Arrows represent the transition time of the respective signals.

Discussion

In this study, we have developed a novel assay platform for real-time imaging of secretion at the single cell level at 1-min intervals. The dynamics of cytokine secretion against external stimuli have conventionally been investigated using a bulk population of cells with the same phenotype, based on the premise that these cells always display uniform responses. However, contrary to this premise, we have observed a wide distribution of onset time for IL-1β release triggered by ATP stimulation from individual human peripheral blood monocytes. Temporal heterogeneities at the single cell level have been demonstrated by many studies, but have been limited to intracellular processes, e.g. intracellular calcium elevation[22]. Our results indicated that extracellular reactions, such as protein secretion, were also chronologically heterogeneous at the single cell level. Furthermore, we successfully performed simultaneous measurement of cell membrane integrity and IL-1β release, indicating that our platform allowed for elucidation of the chronological relationship between intracellular process and the extracellular reaction at the single-cell level.

Imaging methods for secretion dynamics have been poorly developed for two primary reasons: First, secreted molecules disperse too rapidly in solution for efficient onsite monitoring. Second, a molecule of interest must be tagged by sensing moieties, but the tagging processes for molecular visualization are often accompanied with greater risks of generating artifacts, including functional modifications. Indeed, this latter point is the most serious limitation of live-cell imaging in general. The platform developed in this study permitted us to bypass such issues by immobilizing and labelling target molecules in the extracellular space. The detection strategy offers an advantage in its non-invasive monitoring of the physiological response of living cells, including clinical samples. A similar methodology with a label-free technique based upon nanoplasmonic imaging has been developed, although it is only applicable to up to three cells per experiment[23]. Sandwich FIA-based assay is expected to be a more sensitive and specific approach for small molecules like cytokines than the plasmonic approach, since the plasmonic signal is proportional to the molecular weight of the binding molecule.

Our platform uses MWAs that effectively trap floating cells as well as secreted cytokine molecules. This compartmentalization permitted integration of independently isolated single cells within a small area to increase the number of observable cells. More specifically, observation of a large number of cells made it feasible to perform statistical analyses on a small population of secreting monocytes. The open architecture of this device is well suited for cell manipulation using conventional tools, allowing for complex experimental arrangements. Additionally, the open architecture was beneficial for the maintenance of cellular physiology, because prolonged isolation within closed microwells may influence cellular conditions, e.g. oxygen starvation[24]. In this work, MWA chips were fabricated with PDMS, suitable for live cell imaging because of its biocompatibility[25]. PDMS offers low cost and fast processing in fabrication of the MWA chip. The only inconvenience was its higher refractive index than that of water, requiring a higher critical angle of the incident light for TIRFM. We resolved the issue by using an objective lens of high numerical aperture to achieve incidence angles greater than the critical angle for a glass/PDMS interface.

In our experiments, the rate of the apparent increase in the TIRF signal was 15 times slower than that of the apparent capture rate of the antigen onto the bottom surface of the MWA chip. This phenomenon was observed probably because (1) the difference in the local concentration of antibodies near the bottom surface and (2) decrease of the unbound antigen by diffusion followed pseudo first-order kinetics with a time constant of approximately 0.9 min (Supplementary Fig. S2). The increase in the concentration of fluorescent detection antibody accelerates the rate of the apparent increase in the TIRF signal while decreasing the detection sensitivity because of elevated background.

The 2,000-molecule detection limit for IL-1β is as low as that reported earlier[6,8]. The average rate of IL-1β secretion from a single monocyte calculated from bulk measurements (Supplementary

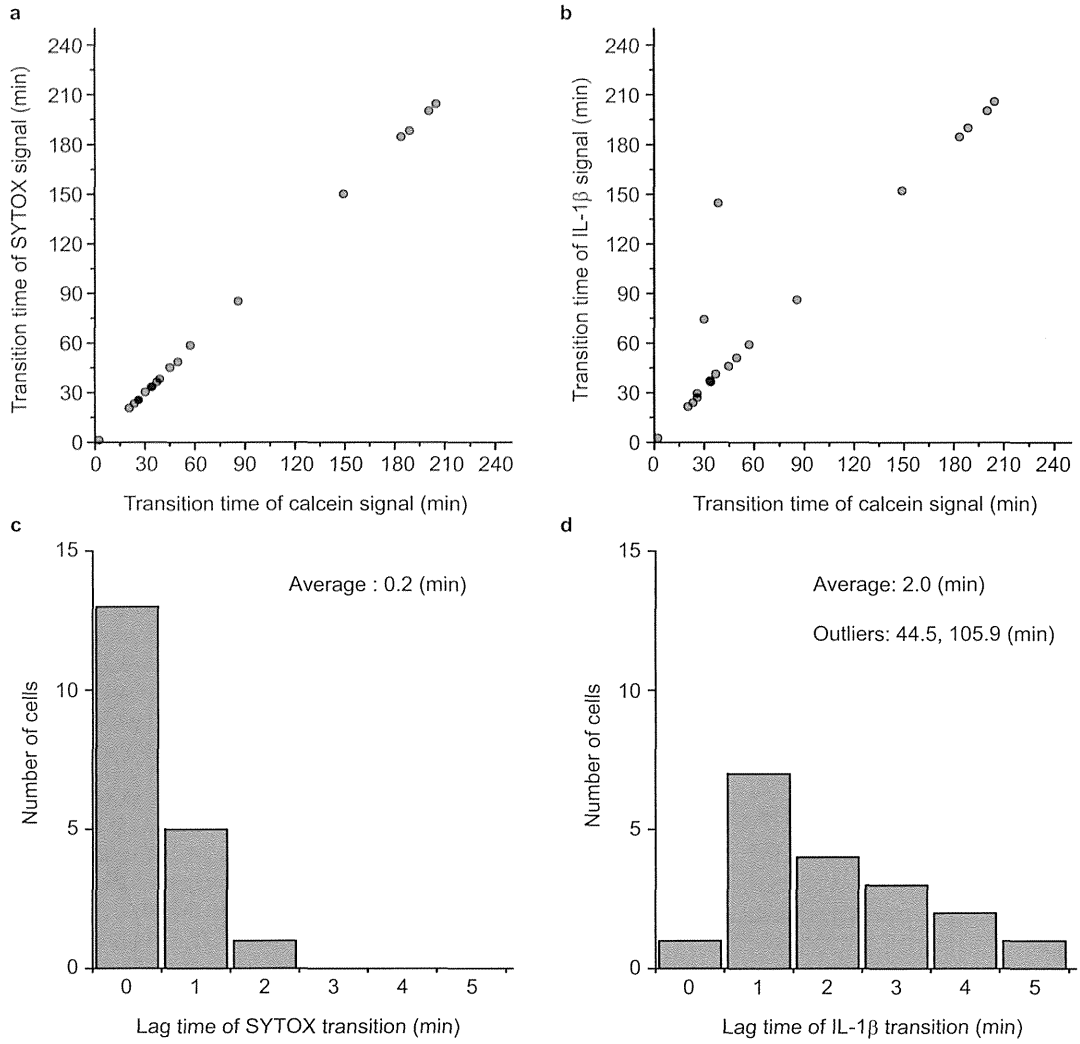

Figure 5 | High concordance of the three transition times observed in individual single cells. (a), (b) Scatter plots of the signal transition times for SYTOX or IL-1β versus calcein. Signal transition occurred virtually simultaneously between calcein, SYTOX, and IL-1β. Each circle represents 20 individual monocytes. (d) Histograms of the lag times of SYTOX or IL-1β signal transition after the calcein disappearance. The lag times of SYTOX were distributed in a narrow range near 0, whereas those of IL-1β showed a wider distribution.

Fig. S6) was approximately 40 molecules/min if all the monocytes continuously secreted IL-1β, implying that it takes more than 50 min to detect IL-1β secretion using our assay system. However, we observed sharp rise of IL-1β signals in some cells, which indicated the massive IL-1β secretion was in a transiently-released manner. This shows the power of our real-time imaging system, which allows the dynamic analysis with improved time resolution as well as analysis for temporal cell-to-cell variations in protein secretion. The concave-down increase of the IL-1β secretion signal also suggested a burst release, rather than continuous secretion of IL-1β. Use of the time constant for association of detection antibody, obtained from the results of a model experiment, enabled estimation of the onset time of a massive burst release of IL-1β with a time resolution of <1 min. The accuracy of onset time estimation was sufficient for identifying the relationship of biophysical phenomena on a minute-based time scale. Smaller time intervals of data acquisition improve the accuracy of curve fitting within a predetermined time window of 5 min, but simultaneously reduce the number of observable microwells during a single cycle of scanning. The nonequilibrium characteristics of the antigen-antibody interaction in the open structure made it difficult to establish a series of concentration standards, but were considered an acceptable trade-off for long-term monitoring of cellular activities.

In addition to previous studies[15,16], our snapshot measurement of IL-1β secretion from monocytes stained with live/dead indicators demonstrated that most of the IL-1β–secreting cells were dead. These observations allow for several interpretations, because the chronological relationship between IL-1β release and the change in calcein/SYTOX staining remained unknown. However, our real-time monitoring experiment showed that IL-1β release always occurred after calcein/SYTOX transition. Since the monitored cells were prepared in the presence of glycine[16], both the calcein/SYTOX transition and IL-1β release were likely caused by pore formation on the plasma membrane, and not by cytolysis[16,17]. Two phases of SYTOX influx were observed during and after ATP administration to monocytes, suggesting multiple cell-permeable processes, such as the ATP-dependent opening of a P2X7 pore allowing for the passage of molecules of up to 900 Da in size[19,26] and large pore formation mediated by caspase 1[20]. Moreover, our analysis of high temporal resolution uncovered a several-minute lag between calcein/SYTOX transition and IL-1β release. This lag time suggested that the calcein/SYTOX-permeable

cells require another process to release IL-1β, a process that remains to be elucidated.

The cytokine secretion dynamics in monocytes described herein implies that cell-cell communication via cytokines also varies widely with regard to timing. Further studies are required to clarify the manner in which heterogeneous cell-cell communication affects the maintenance of homeostasis of the immune system under various complex physiological situations, such as T-helper subset differentiation[27] and the switch from acute resolving to chronic persistent inflammation[28]. The establishment of the real-time secretion assay platform described in this study opens the way to addressing these issues through the monitoring of cytokine secretion dynamics in parallel with intracellular events at single-cell resolution.

Methods

Reagents. The DuoSet ELISA Development System was purchased from R&D Systems (Minneapolis, MN, USA), and the set of capture and detection antibodies was used for sandwich immunoassays for human IL-1β (DY201). Human IL-6 monoclonal antibody (clone 6708; MAB206) and human IL-6 biotinylated affinity-purified polyclonal antibody (BAF206) were also purchased from R&D Systems. Adenosine 5′-triphosphate disodium salt hydrate (ATP, A7699) and lipopolysaccharides from *Escherichia coli* 055:B5 (LPS, L4524) were purchased from Sigma-Aldrich (St. Louis, MO, USA). Lipidure BL802, a water-soluble polymer of 2-methacryloyloxy ethyl phosphorylcholine, was purchased from NOF Corporation (Tokyo, Japan). Calcein AM (C3099) and SYTOX Blue nucleic acid stain (S11348) were purchased from Life Technologies (Carlsbad, CA, USA). CF660R streptavidin was purchased from Biotium (29040; Hayward, CA, USA). Dimethyl pimelimidate-2HCl (DMP, 21666) was purchased from Thermo Fisher Scientific (Rockford, IL, USA). Foetal bovine serum (FBS, s1560) was purchased from Biowest (Nuaillé, France).

Cell culture. The incubation of cells was performed in a CO_2 incubator at 37°C in a humidified atmosphere with 5% CO_2, unless otherwise indicated. For the isolation of human peripheral blood monocytes, 20 mL of venous blood was drawn from a healthy donor after obtaining institutional approval of the ethical committee of the Kyoto University Hospital, in accordance with Declaration of Helsinki. Monocytes from different donors were used for different experiments. The cell fraction was separated with Lymphoprep (Axis-Shield, Dundee, UK) according to the manufacturer's instructions. $CD14^+$ monocytes were sequentially purified by MACS (Miltenyi Biotec, Bergisch Gladbach, Germany) with a negative selection reagent (i.e. monocyte isolation kit II) and a positive selection reagent (i.e. CD14 microbeads). The isolated monocytes were incubated overnight in RPMI medium containing 10% FBS.

Optical arrangement. All measurements were performed with a completely automated inverted microscope (ECLIPSE Ti-E; Nikon, Tokyo, Japan) equipped with a high NA 60× objective lens (TIRF 60 × H; NA, 1.49; Nikon). The microscope was customized to introduce external laser beams (635 nm; Radius 635-25; Coherent, Santa Clara, CA, USA) at the indicated incident angle to actualize TIRF illumination. The following sets of excitation (Ex) and emission (Em) filters and a dichroic mirror (DM) were used with a high-pressure xenon lamp: for SYTOX, Ex = FF01-448/20-25, Em = FF01-482/25-25, and DM = Di02-R442-25x36; and for calcein, Ex = FF02-472/30-25, Em = FF01-520/35-25, and DM = FF495-Di03-25x36. The following Ex and Em filters and DM were used with the 632 nm laser for the CF660R dye: Ex = FF02-628/40-25, Em = FF01-692/40-25, and DM = FF660-Di02-25x36. These optical filters were purchased from Semrock (Rochester, NY, USA). Each image was projected on an EM-CCD camera (ImagEM C9100-13; Hamamatsu Photonics K.K., Sizuoka, Japan) through a 0.7× lens (C-0.7x DXM Relay Lens; Nikon). A stage-top incubator (ONICS; Tokai Hit Co., Shizuoka, Japan) was used to control temperature, humidity, and gas concentration.

MWA chips. MWA chips were prepared from PDMS and microscopic-grade coverslips. The PDMS MWA chip was prepared as follows: A thin PDMS sheet, consisting of a 50 × 50 array of 50-μm or 70-μm through-holes with 100-μm centre-to-centre spacing and 80-μm thickness, was purchased from Fluidware Technologies (Saitama, Japan). The PDMS sheet and a glass slide were permanently bonded together after the contact surfaces between them were plasma-treated (SEDE-PFA; Meiwafosis, Tokyo, Japan). The bare glass surfaces that now functioned as the bottom of the microwells after bonding were aminated with Vecatabond Reagent (SP-1800; Vector Laboratories, Burlingame, CA, USA). The chip was mounted on a coverslip holder (Attofluor cell chamber, A7819; Life Technologies) adjacent to another PDMS block (Sylgard184; Dow Corning Toray, Tokyo, Japan) with an 8-mm diameter through-hole that served as a reservoir well. The interstices between the PDMS-glass chip and the PDMS block were filled with uncured PDMS. The integrated chip was baked at 130°C for 3 h.

A 100-μL mixture of capture antibodies (100 μg/mL) and dimethyl pimelimidate-2HCl (DMP; 7 mg/mL) was loaded onto the aminated glass surface to fix the capture antibody. The surface was blocked with monoethanolamine (0.1 M, pH 8.2) and Lipidure reagent (0.2% [w/v]), and stored at 4°C until use.

Preparation of detection medium. Detection antibody labelled with biotin was coupled with CF-labelled streptavidin at 1 : 10 molar ratios at room temperature in the dark for 3 h. Unoccupied sites on streptavidin were blocked with excess dPEG4-biotin acid (10199; Quanta BioDesign, Ltd., Powell, OH, USA). Unconjugated streptavidin and dPEG4-biotin were removed by ultrafiltration (Amicon Ultra-0.5, 100 kDa; Merck Millipore, Billerica, MA, USA). The detection media contained prepared CF-labelled detection antibody (30 nM), BSA (2.5% [w/v]), and the indicated combination of the following additives (with the final concentrations): SYTOX (0.8 μM), glycine (5 mM), LPS (1 μg/mL), and/or ATP (5 mM).

Handling and treatment of cells. Monocytes were stimulated with LPS for 3 h and incubated with 0.4 μM Calcein AM for 15 min before IL-1β secretion analysis on a PDMS MWA chip. The cells were washed with fresh medium and recovered from the bottom of 96-well plates by gentle pipetting. Approximately 2,000 cells were introduced into an MWA chip and allowed to settle by gravity for 10 min in a CO_2 incubator. Next, the medium was replaced with the detection medium containing SYTOX, glycine, and LPS. The cells were first monitored for 20 min before ATP stimulation; after ATP administration, monitoring was resumed during the 10-min incubation period. The medium was then replaced with fresh detection medium containing SYTOX, glycine, and LPS. Measurements were then resumed and continued for 4 h.

Time-resolved monitoring of cytokine secretion from stimulated monocytes. Ten positions were selected in order to include as many single cell-containing microwells as possible. Monocytes in the selected position of microwells were monitored at 1-min intervals by multichannel microscopy, i.e. DIA images, epifluorescence images for calcein and SYTOX, and TIRF images for CF660R for cytokine secretion at controlled temperature and gas concentrations. The MFIs of each microwell at each time point were measured with the NIS Elements imaging software.

Transition time estimation of calcein, SYTOX and IL-1β signals obtained from LPS/ATP stimulated monocytes. The transition time of calcein disappearance, SYTOX influx, and IL-1β release were detected by data analysis software (Origin 8.6; OriginLab Co., Northampton, MA, USA) by using the following equations:

$$I_c(t) = \begin{cases} I_{c0} + I_{c1} + m_c t & , \ t < t_{c0} \\ I_{c0} + (I_{c1} + m_c t_{c0}) \exp\{-(t - t_{c0})/\tau_c\}, & t \geq t_{c0} \end{cases} \quad (1)$$

for calcein disappearance,

$$I_s(t) = \begin{cases} I_{s0} + m_s t & , \ t < t_{s0} \\ I_{s0} + m_s t + I_{s1}[1 - \exp\{-(t - t_{s0})/\tau_s\}], & t \geq t_{s0} \end{cases} \quad (2)$$

for SYTOX influx, and

$$I_i(t) = \begin{cases} I_{i0} + m_i t & , \ t < t_{i0} \\ I_{i0} + m_i t + I_{i1}[1 - \exp\{-(t - t_{i0})/\tau_i\}], & t \geq t_{i0} \end{cases} \quad (3)$$

for IL-1β release, where $I(t)$ represents intensity, I_0 represents the background, m represents intensity drift, I_1 represents amplitude, t_0 represents transition time, and τ represents the time constant of exponential decay for each fluorescence signal. The subscripts c, s, and i of each parameter indicate calcein, SYTOX, and IL-1β labelling, respectively. The time constant of IL-1β (τ_i) was determined from a supplementary experiment with recombinant IL-1β (Fig. 2). The IL-1β secretion dataset was fitted by equation (3).

1. Gnecchi, M., Zhang, Z. P., Ni, A. G. & Dzau, V. J. Paracrine Mechanisms in Adult Stem Cell Signaling and Therapy. *Circ Res* **103**, 1204–1219 (2008).
2. Lander, A. D. How Cells Know Where They Are. *Science* **339**, 923–927 (2013).
3. Stastna, M. & Van Eyk, J. E. Secreted proteins as a fundamental source for biomarker discovery. *Proteomics* **12**, 722–735 (2012).
4. Rothenberg, E. V. Cell lineage regulators in B and T cell development. *Nat Immunol* **8**, 441–444 (2007).
5. Lacy, P. & Stow, J. L. Cytokine release from innate immune cells: association with diverse membrane trafficking pathways. *Blood* **118**, 9–18 (2011).
6. Ma, C. *et al.* A clinical microchip for evaluation of single immune cells reveals high functional heterogeneity in phenotypically similar T cells. *Nat Med* **17**, 738–743 (2011).
7. Love, J. C., Ronan, J. L., Grotenbreg, G. M., van der Veen, A. G. & Ploegh, H. L. A microengraving method for rapid selection of single cells producing antigen-specific antibodies. *Nat Biotechnol* **24**, 703–707 (2006).
8. Han, Q., Bagheri, N., Bradshaw, E. M., Hafler, D. A., Lauffenburger, D. A. & Love, J. C. Polyfunctional responses by human T cells result from sequential release of cytokines. *P Natl Acad Sci USA* **109**, 1607–1612 (2012).
9. Sasuga, Y. *et al.* Single-cell chemical lysis method for analyses of intracellular molecules using an array of picoliter-scale microwells. *Anal Chem* **80**, 9141–9149 (2008).
10. Salehi-Reyhani, A. *et al.* A first step towards practical single cell proteomics: a microfluidic antibody capture chip with TIRF detection. *Lab Chip* **11**, 1256–1261 (2011).
11. Stanley, A. C. & Lacy, P. Pathways for Cytokine Secretion. *Physiology* **25**, 218–229 (2010).

12. Dinarello, C. A. Biologic basis for interleukin-1 in disease. *Blood* **87**, 2095–2147 (1996).
13. Fujisawa, A. *et al.* Disease-associated mutations in CIAS1 induce cathepsin B-dependent rapid cell death of human THP-1 monocytic cells. *Blood* **109**, 2903–2911 (2007).
14. Tanaka, T. *et al.* Induced pluripotent stem cells from CINCA syndrome patients as a model for dissecting somatic mosaicism and drug discovery. *Blood* **120**, 1299–1308 (2012).
15. Bergsbaken, T., Fink, S. L. & Cookson, B. T. Pyroptosis: host cell death and inflammation. *Nat Rev Microbiol* **7**, 99–109 (2009).
16. Eder, C. Mechanisms of interleukin-1beta release. *Immunobiology* **214**, 543–553 (2009).
17. Lopez-Castejon, G. & Brough, D. Understanding the mechanism of IL-1beta secretion. *Cytokine Growth Factor Rev* **22**, 189–195 (2011).
18. Mariathasan, S. *et al.* Cryopyrin activates the inflammasome in response to toxins and ATP. *Nature* **440**, 228–232 (2006).
19. Ward, J. R. *et al.* Temporal Interleukin-1 beta Secretion from Primary Human Peripheral Blood Monocytes by P2X7-independent and P2X7-dependent Mechanisms. *Journal of Biological Chemistry* **285**, 23145–23156 (2010).
20. Fink, S. L. & Cookson, B. T. Caspase-1-dependent pore formation during pyroptosis leads to osmotic lysis of infected host macrophages. *Cell Microbiol* **8**, 1812–1825 (2006).
21. Verhoef, P. A., Kertesy, S. B., Estacion, M., Schilling, W. P. & Dubyak, G. R. Maitotoxin induces biphasic interleukin-1beta secretion and membrane blebbing in murine macrophages. *Mol Pharmacol* **66**, 909–920 (2004).
22. Roy, S. S. & Hajnoczly, G. Calcium, mitochondria and apoptosis studied by fluorescence measurements. *Methods* **46**, 213–223 (2008).
23. Raphael, M. P., Christodoulides, J. A., Delehanty, J. B., Long, J. P. & Byers, J. M. Quantitative Imaging of Protein Secretions from Single Cells in Real Time. *Biophys J* **105**, 602–608 (2013).
24. Molter, T. W. *et al.* A New Approach for Measuring Single-Cell Oxygen Consumption Rates. *IEEE Trans Autom Sci Eng* **5**, 32–42 (2008).
25. Belanger, M. C. & Marois, Y. Hemocompatibility, biocompatibility, inflammatory and in vivo studies of primary reference materials low-density polyethylene and polydimethylsiloxane: A review. *J Biomed Mater Res* **58**, 467–477 (2001).
26. Ferrari, D. *et al.* The P2X(7) receptor: A key player in IL-1 processing and release. *Journal of Immunology* **176**, 3877–3883 (2006).
27. Zhu, J. F. & Paul, W. E. Heterogeneity and plasticity of T helper cells. *Cell Res* **20**, 4–12 (2010).
28. Nathan, C. & Ding, A. H. Nonresolving Inflammation. *Cell* **140**, 871–882 (2010).

Acknowledgments

We thank Katsuyuki Shiroguchi (RIKEN) and Hirotsugu Oda (Kyoto Univ.) for critical reading of the manuscript. This work was partly supported by the Special Postdoctoral Researchers Program of RIKEN, by a Grant-in-Aid for Young Scientists (B) (no. 23770189, to Y.S.), a Grant-in-Aid for Scientific Basic Research (C) (no. 25440074, to Y.S.) and for Scientific Basic Research (S) (no. 23226010, to S.S.) from MEXT, Japan.

Author contributions

Y.S., Y.H. and O.O. conceived the methods described; Y.S. and M.Y. set up the optical instruments; A.N., J.M. and S.S. contributed to the technical development of the MWA chip; Y.S. and N.S. prepared MWA chips; K.I., R.N. and T.H. performed and supervised clinical sample preparation; and Y.S. performed imaging experiments and analysis. The manuscript was prepared by Y.S., M.Y., and O.O. after discussion with all the authors.

Additional information

Supplementary information accompanies this paper at http://www.nature.com/scientificreports

Competing financial interests: The authors declare no competing financial interests.

How to cite this article: Shirasaki, Y. *et al.* Real-time single-cell imaging of protein secretion. *Sci. Rep.* **4**, 4736; DOI:10.1038/srep04736 (2014).